Wiley
International Journal of Energy Research
Volume 2024, Article ID 3819821, 26 pages
https://doi.org/10.1155/2024/3819821

WILEY

Research Article

Characteristic of Premixed Hydrogen/Air Tubular Flames in Microcombustor: Effects of Stimulated and Unstimulated Inlet Conditions on Flame Dynamics

Alireza Alipoor[1] **and Pouyan Abbaspour**[2]

[1]*School of Mechanical Engineering, Shiraz University, Shiraz 71348-51154, Iran*
[2]*Department of Mechanical Engineering, Shahid Chamran University of Ahvaz, Ahvaz, Iran*

Correspondence should be addressed to Alireza Alipoor; a.alipoor@shirazu.ac.ir

Received 19 March 2024; Revised 27 April 2024; Accepted 4 May 2024; Published 30 May 2024

Academic Editor: Weiwei Han

The present study investigates the characteristics and periodic behavior of H_2/air tubular flames in a 1 mm diameter microtube under exciting and nonexciting inlet conditions. Under unstimulated inlet conditions, increasing inlet velocity positively impacted flow stratification and self-sustaining of the tubular flames, leading to higher maximum temperatures within the flame kernel due to reduced flow temperature gradients near the wall. Conversely, under stimulated conditions, varying excitation amplitudes resulted in two flame propagation modes: flame with semi-repetitive extinction/ignition (FSREI) and pulsating flame, observed across different exciting amplitude ranges. It was found that the formation of recirculation fields generated by negative propagation speed temporarily stored the released heat of combustion and prevented it from extinguishing in the flowing phase. From the kinetics point of view, the maximum reaction rate during the pulsating mode belongs to $H + O_2 = HO_2$, while competition between $H + O_2 = HO_2$ and $H_2 + OH = H_2O + H$ occurred in the FSREI mode. Results revealed that in the pulsating mode, fluctuations in mass fractions of the heavier species are more considerable near the outlets. However, radical mass fraction fluctuations were significant near the inlet slot in pulsating mode.

1. Introduction

The main obstacles encountered in small-scale combustor design are inadequate residence time for complete combustion and flame stability, resulting in quenching due to the high surface area-to-volume ratio [1]. Variation in the time scales of small-scale combustor will significantly enrich the dynamics of combustion phenomena. It results in rich phenomena with various flame dynamics such as repetitive ignition/extinction [2–7], split flame [8, 9], spinning flame [10, 11], steady asymmetric flame [12], oscillating and pulsating flames [13–17], and other flame patterns [17–24].

Nakamura et al. [25] investigated the detailed behavior of flame with repetitive extinction/ignition (FREI) in a heated wall microchannel. The bifurcation of the heat release rate peak and negative propagation speed of the bifurcated peak were successfully captured in the ignition and weak flame phases. Alipoor and Mazaheri [6] demonstrated that the formation of a recirculation zone adjacent to the walls causes the flame to bifurcate in FREI. Also, they showed that the increase of heavier species, such as H_2O, HO_2, and H_2O_2, between the two flame fronts in FREI, absorbs more released heat of combustion, leading decrease in flow temperature, and finally, flame bifurcates [7]. Asymmetric FREI was also observed in a 5 mm microtube by Ayoobi and Schoegl [26]. Spinning, rotating, and pulsating flames were observed by Malushte and Kumar [27] in their experiments on microcombustors with heat recirculation zone. Their results showed that the pulsating flame mode vanishes from a lean to a rich mixture by decreasing the combustor diameter. Lee S. and Lee B.J. [28] investigated the effect of wall temperature conditions on the dynamics of H_2/air flames in a square microchannel. FREI, pulsating, laterally oscillating flame, and steady flame propagation modes appeared

according to the thermal condition of the wall. Edacheri et al. [29] investigated the FREI behavior of premixed C1-C4 alkane/air flames by adding H_2 to their mixture. Results illustrated that bifurcation disappeared in CH_4/air for H_2 concentrations higher than 20%, leading to a decrease in FREI frequency. Ren et al. [30] explored how adding hydrogen affects natural gas combustion characteristics. Results showed that increasing hydrogen mole fractions enhances laminar burning speed and adiabatic flame temperatures of methane and other alkanes. Additionally, active radical production correlates strongly with laminar burning velocity. In another study, Ren et al. [31] showed that CO_2 has a grater chemical impact on laminar burning velocity and adiabatic flame temperature. Xiang et al. [32] investigated the impact of hydrogen as a diluent on methane and ethane combustion. Results showed that H_2 inhibits chemical reactions, leading to decreased net heat released rates, while accelerating others. Key elementary reactions identified $H + O_2 = OH + O$ and $CO + OH$.

The origin of these relatively complex dynamics for flame propagation on a small scale is inherent, especially for lean conditions, and has not been commonly observed in conventional combustion systems. In this regard, various shapes for microcombustors have been proposed to prevent instabilities, extend flammability limits, and consequently, make combustors more applicable. Kunte et al. [33] investigated the performance characteristics of a novel spiral geometry for catalytic C_3H_8/air combustion. Zuo et al. [34] numerically studied an improved counterflow double-channel microcombustor fueled with hydrogen for enhancing thermal performance. Bani et al. [35] used a porous medium to maintain flame in the combustor for a more extensive range. Ansari and Amani [36] proposed a new configuration for the combustor by focusing on the presence of a bluff body and baffle in the combustor. Yang et al. [37] compared thermal performance in a swirling microcombustor under premixed and nonpremixed conditions. Yang et al. [38] and Biswas et al. [24] studied combustion characteristics in converging-diverging channels. Yang et al. [39] analyzed the flame stability of premixed H_2/air mixtures in a swirl microcombustor. Abbaspour and Alipoor [40] study showed that the presence of wavy walls can extend the upper flammability limit of lean premixed H_2/air flames up to three times in comparison to smooth walls. Moreover, few types of research have been conducted on wavy wall microcombustors [41–43].

To improve problems regarding combustion in the microscale, tubular flames can be suggested with proven satisfactory features that have not been studied extensively. Tubular flames are defined as circular flames in cross-section and long in the perpendicular direction of flow [44]. These flames could be created in swirl burners where the combustible mixture enters through the tangential direction in premixed [45] or nonpremixed [46] conditions instead of the axial direction. Circumferential motion causes to create a rotating flow field in the combustor. It has been proven that tubular flames have higher stability than other types of flames because of rotational flow inside the combustor. The flame is aerodynamically stable according to the Rayleigh stability criterion as it is formed in a rotating flow field [47]. Also, the flame is enclosed by an inlet (or injected) combustible mixture, and it has no contact with the wall. Therefore, heat loss behind the flame front in the radial direction can be reduced or even negligible. These interesting features for tubular flames regarding stability issues can introduce tubular flames as a good candidate for use in microcombustors. Shimokuri et al. [48] showed that propagation of CH_4/air and C_3H_8/air tubular flames could be accessible in microcombustors of 3.6 mm diameter. Their study determined CH_4/air propagation limits for swirling and nonswirling inlet conditions. It was found that tubular flame can firmly stabilize in the microcombustor as inlet velocity increases from the value at which the flame is completely blown out in the nonswirling case. Shimokuri et al. [49] extended their study by using AR, N_2, He, and CO_2 as diluents. It was found that Ar-dilution has the most expansive propagation limit than others. Also, they observed that the Lewis number could strongly affect flame propagation in small diameters. Because the flame is convex in shape towards the unburned gas, the flame intensifies at the tip for cases in which $Le < 1$ (i.e., for Ar-dilution and N_2-dilution in fuel-rich conditions). In contrast, the flame weakens at the tip for cases where $Le > 1$ (i.e., for N_2-dilution and Ar-dilution in lean mixtures). Therefore, propagation limits become narrower in cases in which the Lewis number is more significant than unity.

Due to the ability of the miniaturized combustion chambers to be installed on some mobile instruments, the effect of some environmental factors, such as acceleration or impacts (as a result of change in momentum), can serve as the driving force of the flame perturbations. Also, the high tendency of flame to show unsteady behavior near the quenching conditions can provoke these perturbations. As the literature review showed, there is a research gap in the field of microcombustion about flame dynamics affected by these perturbations. In fact, attention has been focused on other factors such as wall thermal conditions or material, fuel/air conditions, and bluff body as driving forces of flame oscillations. For these reasons, there is enough motivation to investigate the flame response to the microcombustion chamber perturbations. Also, the study on the premixed tubular flames in microcombustion chambers has been restricted to references [48, 49] only for CH_4/air and C_3H_8/air, and the lack of research on the H_2/air microtubular flames is quite evident. Moreover, exclusive features of the tubular flames with their high level of stability are persuasive enough to examine them more in microcombustion applications.

With these in mind, the present study is aimed at achieving two main goals. Firstly, to investigate premixed H_2/air tubular flames near quenching conditions to examine such flame's potential in microcombustion chambers. The second objective is to identify the tubular flame dynamics under perturbations. Therefore, the inlet passages, which are referred to as slots, are incorporated to introduce a fresh mixture circumferentially and form a tubular flame inside the microtube. The microtube diameter is chosen to be 1 mm, close to the quenching diameter of hydrogen, to examine the potential of the premixed H_2/air tubular flames

near the quenching conditions. Various methods exist for modeling flame perturbations in practice and theoretical contexts.

To avoid coupling of acoustic and reactive flow equations and related complications in numerical studies, the driving force for flame perturbations is typically modeled using fluctuating boundary conditions at the inlet [50, 51]. This approach, employed in previous research, is also adopted in the present study to model the driving force of flame perturbations. Consequently, the study investigates the flame's response to forcing excitation, including variations in frequency and amplitude. Additionally, flame responses are examined from both hydrodynamics and kinetics perspectives.

This paper is organized in the following manner. The subsequent section introduces the assumptions, governing equations, geometric details, and numerical procedures. Subsequently, the results are discussed. Initially, the characteristics of tubular flames without forcing excitation are examined. Following that, the response of tubular flames to forcing excitation is explored. Lastly, the fundamental conclusions of this study are summarized.

2. Numerical Approach

2.1. Governing Equations. Governing equations consist of the conservation of mass, momentum, energy, species, and ideal gas equation of state, formulated using the low Mach number approach. In this study, simulations are conducted in three dimensions, unsteady, and laminar. Surface reactions are not included. Radiative heat transfer between surfaces is disregarded. The gas mixture is assumed to behave as an ideal gas, with the implementation of a multispecies transport model. Consequently, the governing equations based on the low Mach number approach and aforementioned assumptions are as follows:

Conservation of mass:

$$\frac{\partial \rho}{\partial t} + \nabla.(\rho \boldsymbol{u}) = 0. \tag{1}$$

Conservation of momentum:

$$\rho\left(\frac{\partial \boldsymbol{u}}{\partial t} + \boldsymbol{u}.\nabla \boldsymbol{u}\right) = -\nabla P_d + \nabla.(\mu S). \tag{2}$$

Conservation of energy:

$$\rho C_P\left(\frac{\partial T}{\partial t} + \boldsymbol{u}.\nabla T\right) = \nabla.(\lambda \nabla T) - \sum_{i=1}^{N} h_i \dot{\omega}_i - \rho\left(\sum_{i=1}^{N} C_{P,i} Y_i V_i\right).\nabla T. \tag{3}$$

conservation of species:

$$\rho\left(\frac{\partial Y_i}{\partial t} + \boldsymbol{u}.\nabla Y_i\right) = -\nabla.(\rho Y_i V_i) + \dot{\omega}_i. \tag{4}$$

Ideal gas equation of state:

$$P_t = \rho \frac{R}{\bar{W}} T, \tag{5}$$

where ρ, $\boldsymbol{u}$, μ, $\bar{W}$, λ, P_d, and P_t represent density, velocity vector, dynamic viscosity, mean molecular weight in the mixture, the thermal conductivity of the mixture, hydrodynamic pressure, and thermodynamic pressure, respectively. The stress tensor is S computed using the following equation.

$$S = \nabla \boldsymbol{u} + (\nabla \boldsymbol{u})^T - \frac{2}{3}(\nabla \boldsymbol{u})I, \tag{6}$$

where I is the identity matrix. Additionally, $\dot{\omega}_i$, Y_i, and V_i represent the rate of $\boldsymbol{i}^{\text{th}}$ species production/destruction, mass fraction of the $\boldsymbol{i}^{\text{th}}$ species, and diffusive velocity of the $\boldsymbol{i}^{\text{th}}$ species, respectively. V_i is calculated using Equation (7) as follows:

$$V_i = V_i^* + V_c, \tag{7}$$

where V_i^* is calculated using the kinetic theory of gases according to Equation (8), considering only mixture-averaged diffusion [11]. Additionally, V_c is the correction velocity [52], introduced to ensure total mass conservation, and is determined by Equation (9).

$$V_i^* = -\left(\frac{D_{\text{im}}}{X_i}\right)\nabla X_i, \tag{8}$$

$$V_c = -\sum_{i=1}^{N} Y_i V_i^*, \tag{9}$$

where D_{im} and X_i are the average diffusivity of the $\boldsymbol{i}^{\text{th}}$ species in the mixture m and mole fraction of the $\boldsymbol{i}^{\text{th}}$ species. D_{im} is calculated from Equation (10) based on the Chapman-Enskog theoretical-empirical description of binary mixtures of gases at low to moderate pressures [53].

$$D_{\text{im}} = \frac{1 - \chi_i}{\sum_{j \neq i}^{N}\left(\chi_j / D_{\text{ij}}\right)} \quad \text{for} \quad i = 1, 2, 3, \cdots, N-1, \tag{10}$$

$$D_{\text{ij}} = \frac{0.0266 T^{3/2}}{\text{P}\text{W}_{\text{ij}}^{1/2} \sigma_{\text{ij}}^2 \Omega_D}, \tag{11}$$

$$W_{\text{ij}} = 2\left[\left(\frac{1}{W_i}\right) + \left(\frac{1}{W_j}\right)\right]^{-1}; \sigma_{\text{ij}} = \frac{\sigma_{\text{i}} + \sigma_{\text{j}}}{2}, \tag{12}$$

$$\Omega_D = \frac{A}{(T^*)^B} + \frac{C}{\exp(\text{DT}^*)} + \frac{E}{\exp(\text{FT}^*)} + \frac{G}{\exp(\text{HT}^*)}, \tag{13}$$

$$A = 1.06036, \tag{14}$$

$$\text{B} = 0.15610, \tag{15}$$

$$\text{C} = 0.19300, \tag{16}$$

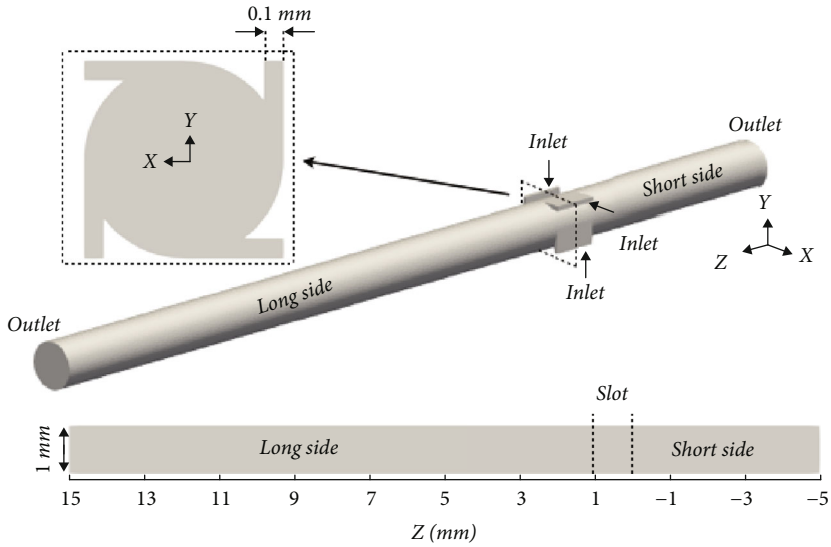

Figure 1: Geometry and dimensions of the suggested microtube with YZ-plane and XY-plane cross-sections.

$$D = 0.47635, \tag{17}$$

$$\mathrm{E} = 1.03587, \tag{18}$$

$$\mathrm{F} = 1.52996, \tag{19}$$

$$G = 1.76474, \tag{20}$$

$$\mathrm{H} = 3.89411, \tag{21}$$

$$T^* = \frac{\mathrm{k_B T}}{\left(\varepsilon_\mathrm{i}\varepsilon_\mathrm{j}\right)^{1/2}}. \tag{22}$$

Also, $\dot{\omega}_i$ in Equation (4) is calculated as follows:

$$\begin{aligned} \dot{\omega}_i &= \sum_{j=1}^{L} \upsilon_{\mathrm{ij}} q_j \quad \text{for} \quad i = 1, 2, \cdots, N, \\ \upsilon_{\mathrm{ij}} &= \left(\upsilon_{\mathrm{ij}}'' - \upsilon_{\mathrm{ij}}'\right), \\ q_j &= k_{fj} \prod_{i=1}^{N} [X_i]^{\upsilon_{\mathrm{ij}}'} - k_{\mathrm{rj}} \prod_{i=1}^{N} [X_i]^{\upsilon_{\mathrm{ij}}''}, \end{aligned} \tag{23}$$

where υ_{ij}' and υ_{ij}'' are the stoichiometric coefficients of i^{th} species in the j^{th} reversible reaction on the reactants and products, respectively. q_j is the reaction rate of the j^{th} reaction. k_{fj} and k_{rj} are the rate constants of j^{th} reaction for the forward and reverse directions, respectively.

2.2. Geometry, Boundary Conditions, and Numerical Procedure. The geometry comprises a microtube with a diameter of a 1 mm and four slots positioned around its circumference, through which a premixed combustible mixture of H_2/air enters the microtube. Figure 1 illustrates a three-dimensional view of the geometry, including cross-sections and dimensions. The geometry is divided into two parts: a long side and a short side. Long side is related to the main part of the combustor and is subjected to a specified temperature boundary condition. To induce flame dynamics with backflow, a short side is included. The inlet slots feature a rectangular cross-section with specified height of 0.1 mm and a length of 1 mm length.

In experimental studies, perturbations are induced at the inlet of a combustion chamber through fluctuations in the inlet conditions. To achieve this, fluctuations are created at a specific frequency and amplitude at the inlet of the combustor. In our numerical simulations, perturbations are applied to the inlet velocity boundary condition using a sinusoidally oscillating function, as defined by Equation (24). Here, U_{inlet} represents the time-averaged bulk velocity at the inlet, A is forcing or exciting amplitude, and F is forcing or exciting frequency. This approach is employed to simulate the stimulated condition, and the velocity boundary condition is utilized to model the inlet excitations.

$$u_{\mathrm{inlet}} = U_{\mathrm{inlet}}[1 + A \sin(2\pi F t)]. \tag{24}$$

Accordingly, two boundary conditions are applied to the inlet velocity. The first is a Dirichlet boundary condition for cases without inlet excitation. The second is a sinusoidally oscillating inlet velocity following Equation (24) for cases considering inlet excitation. For other variables, a zero-Neuman boundary condition is set for pressure, a Dirichlet boundary condition for temperature ($T = 300$ K), and species mass fractions. A no-slip condition is applied for velocity at wall boundaries, along with a zero-Neumann boundary condition for all species mass fractions and pressure. Additionally, a Dirichlet boundary condition of $T = 300$ K is imposed on the short side's wall and $T = 960$ K on the long side's wall. At the outlets, a zero-Neuman boundary condition is applied for all variables ($dT/\mathrm{dn} = 0$, $\mathrm{du/dn} = 0$, and $\mathrm{dy}_i/\mathrm{dn} = 0$), except for pressure, which is set to constant atmospheric pressure. The reaction mechanism employed for H2/air combustion in this study is the detailed mechanism of Kim et al. [54], comprising 9 species and 21 reversible elementary reactions as listed in Table 1. Furthermore, the

Table 1: Detailed reaction mechanism for H_2/O_2 [54].

No.	Reaction	A (mole.cm.K.s)	n	E (kJ/mole)
H_2-O_2 chain reactions				
R1	$H + O_2 = O + OH$	$1.94E + 14$	0.0	68784.96
R2	$O + H_2 = H + OH$	$5.080E + 04$	2.67	26317.36
R3	$H_2 + OH = H_2O + H$	$2.16E + 08$	1.51	14351.12
R4	$O + H_2O = OH + OH$	$2.95E + 06$	2.02	56065.6
H_2-O_2 dissociation/recombination reactions				
R5	$H_2 + M = H + H + M$ $H_2O/12.0/H_2/2.5/$	$4.570E + 19$	-1.40	435136
R6	$O + O + M = O_2 + M$ $H_2O/12.0/H_2/2.5/$	$6.170E + 15$	-0.50	0
R7	$O + H + M = OH + M$ $H_2O/12.0/H_2/2.5/$	$4.720E + 18$	-1.0	0
R8	$H + OH + M = H_2O + M$ $H_2O/12.0/H_2/2.5/$	$2.24E + 22$	-2.0	0
Formation and consumption of HO_2				
R9	$H + O_2(+M) = HO_2(+M)$ LOW/6.70E+19 −1.42 0.0/ TROE/1.0 1E-30 1E+30/ $H_2O/12.0/H_2/2.5/O_2/0.78/$	$4.52E + 13$	0.0	0.0
R10	$HO_2 + H = H_2 + O_2$	$6.62E + 13$	0.0	8911.92
R11	$HO_2 + H = OH + OH$	$1.69E + 14$	0.0	3656.816
R12	$HO_2 + O = OH + O_2$	$1.75E + 13$	0.0	-1661.048
R13	$HO_2 + OH = H_2O + O_2$	$1.90E + 16$	-1.0	0.0
Formation and consumption of H_2O_2				
R14	$HO_2 + HO_2 = H_2O_2 + O_2$ DUP	$4.200E + 14$	0.0	50124.32
R15	$HO_2 + HO_2 = H_2O_2 + O_2$ DUP	$1.30E + 11$	0.0	-6815.736
R16	$H_2O_2(+M) = OH + OH(+M)$ LOW/1.20E+17 0.0 45500/TROE/0.502 1E-30 1E+30/$H_2O/12.0/H_2/2.5/$	$3.0E + 14$	0.0	202756.64
R17	$H_2O_2 + H = H_2O + OH$	$1.0E + 13$	0.0	15020.56
R18	$H_2O_2 + H = HO_2 + H_2$	$4.820E + 13$	0.0	33262.8
R19	$H_2O_2 + O = OH + HO_2$	$9.64E + 06$	2.0	16610.48
R20	$H_2O_2 + OH = H_2O + HO_2$ DUP	$1.000E + 12$	0.0	0
R21	$H_2O_2 + OH = H_2O + HO_2$ DUP	$5.800E + 14$	0.0	39986.488

The rate constant is calculated by $k = AT^n \exp(-E/RT)$. A is the preexponential factor, T is temperature, E is the activation energy, R is the universal gas constant, and n is the temperature exponent. Enhanced third-body efficiencies in reactions R5-R8, R9, and R16 are 12.0 for H_2O and 2.5 for H_2. Reaction pairs (R14 and R15) and (R20 and R21) are duplicates, and the reaction rate is the sum of the two rate expressions. R9 and R16 are pressure fall-off Troe reactions centered at 1.0 and 0.502, respectively (second entries are the low-pressure limits).

mixture-average transport model is utilized for the species diffusion velocities based on the CHEMKIN transport database.

A new OpenFOAM solver called "RITLFOAM" was developed according to the problem requirements. Since the Mach number in the microcombustion problem is low, low-Mach number formulation of Navier-Stokes equations was considered in the mentioned solver. Also, in this scale, molecular phenomenon can be important. So, multispecies transport model is needed to calculate the mass diffusion coefficients of the species. The accuracy of the solver has been extensively investigated in previous works by the authors [6, 12], demonstrating good agreement with the

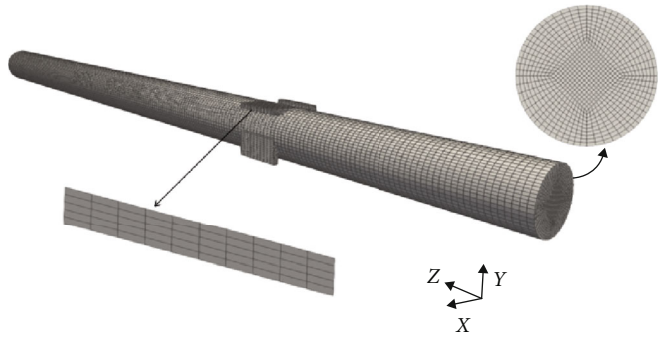

Figure 2: Selected grid of the microtube for numerical study.

experimental results. Additionally, based on the author's published paper, cell size of 10 μm shows independency results from the grid, and this size has consequently been chosen for simulation (Figure 2).

To ensure the appropriate grid and validate the simulation, experimental results from [47] were taken into account. In these experiments, the premixed methane-air mixture enters tangentially from four slots into the combustion chamber and exits axially from the circular ends. Figure 3(a) shows temperature variation in a cross-section of the combustor located 3 millimeters from the end of the combustor. As depicted in Figure 3(a), the simulation results exhibit good agreement with the experimental work of [45]. In Figures 3(a) and 3(b), grid study for the mentioned geometry is illustrated. For this reason, temperature variation has been plotted on the axial line of the combustor for five grids including 93.5 K (i.e., cell size of 30 μm), 135 K (i.e., cell size of 20 μm), 225 K (i.e., cell size of 14 μm), 280 K (i.e., cell size of 10 μm) and 350 K (i.e., cell size of 8 μm). Based on Figure 3(b), it is observed that by increasing the number of grid cells, the simulation is converged to a specific solution. Therefore, cell number of 280 K is suitable for simulation. This cell number verifies the previous author's work about cell size (i.e., cell size of 10 μm).

3. Results and Discussion

In this section, the results are presented and discussed in two parts. The first part examines combustion characteristics under unstimulated inlet conditions, with stream tubes, OH mass fraction iso-level surfaces, velocity, and temperature diagrams illustrating conditions where the flame can be sustained in the microtube. Since the OH radical is one of the active species in the flame front, it is chosen as the indicative of the flame front. The second part investigates tubular flame behavior under stimulated inlet conditions. The results are discussed using diagrams depicting temperature, velocity, species mass fraction amplitude, and contours of OH mass fractions. Additionally, flame propagation types are analyzed from a chemical kinetics perspective.

3.1. Investigation of the Flame Characteristics under the Unstimulated Inlet Condition. The iso-level surfaces of OH mass fraction are depicted in Figure 4 for various inlet velocities at an equivalence ratio of 0.5. Additionally, stream tubes are illustrated to provide further insight into the circulations and flow structures within the microtube. The legends of the stream tubes are color-coded based on the flow velocity. According to the figure, it is observed that for the inlet velocity of 1 m/s, the flame exhibits an elliptical or spherical shape. However, as the inlet velocity increases, the flame elongates in the perpendicular direction, resulting in a tubular flame. Moreover, the mass fraction of OH increases due to the increased inlet mass flow rate resulting from increasing the inlet mass flow rate. At the inlet velocity of U_{inlet} = 1 m/s, the stream tubes remain predominantly parallel throughout the domain, except near the inlet, where the circumferential flow occurs. Hence, the axial velocity component is dominant. Upon increasing the inlet velocity to 6 m/s, the circumferential velocity significantly appears near the slots, leading to the stream tubes being affected, and curled, particularly on the short side. However, the stream tubes remain parallel in the most parts of the long side. Circulations became more robust on the short side as the inlet velocity increases to 9 m/s. Nevertheless, the long side did not show significant circulations except near the slots. No evidence of parallel stream tubes is observed on the short side at the inlet velocity of 9 m/s and 15 m/s. The intensified circulations induce more axial velocity (in the perpendicular direction), leading to further elongation of the flame in the perpendicular direction and maintenance of the flame in the tubular shape.

According to Figures 4(b), 4(c), and 4(d), the flame elongation is more significant towards the short side because the increase in inlet velocity has strengthened the flame and caused to increase of flow velocity versus the burning velocity in the radial direction. Consequently, rather than expanding radially, the flame elongates axially. This is attributed to the intensified circumferential flow surrounding the flame resulting from the enhanced inlet velocity. Additionally, the enhancement of the flame surface leads to an increase in the heat release rate, causing the gas mixture density to rise around the flame. Consequently, the pressure gradient increases due to the density enhancement, ultimately resulting in greater flame acceleration along the shorter side owing to its reduced length. Consequently, the flame appears more elongated on the shorter side, with a sharper tip at U_{inlet} = 15 m/s. Furthermore, the flame tip expands more

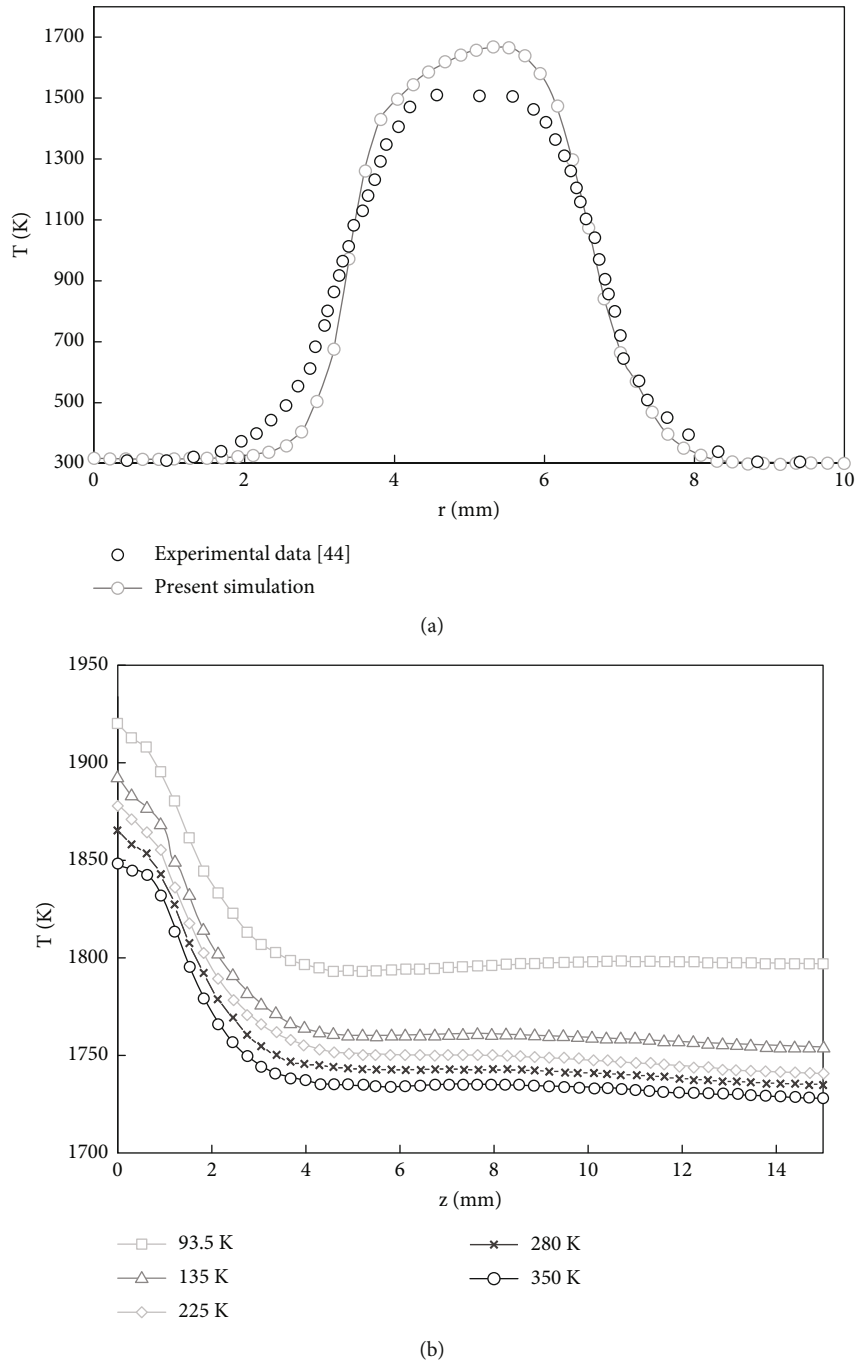

Figure 3: Temperature variations in a cross-section of combustor located 3 millimeters (a) from the end of the combustor and (b) on the axial line of combustor for the experimental data and the present simulation.

towards the shorter side, as depicted in Figure 4(d). owing to the heightened swirl flow intensity and burning velocity enhancement. The intensified swirl flow effects are amplified by the increase in inlet velocity, causing a notable rise in the centrifugal acceleration of the reactive flow. At positions $Z = 0$ to $Z = -1$ mm, where there is no incoming flow, so the effect of the centrifugal forces intensifies and pulls the reactive flow towards the wall. By increasing of heat release rate, burning velocity increases, leading to flame expansion towards the unburned mixture near the wall.

To further investigate the impact of swirl flow, diagrams illustrating the circumferential velocity u_θ and radial velocity u_r are plotted along the x-axis (radial direction) on the cross-sections at the positions of $Z = -1$ mm and $Z = 1.5$ mm in Figures 5(a), 5(b), 5(c), and 5(d), respectively. According to the figure, circumferential velocity is zero at the center of the microtube ($X = 0$) and at the wall ($X = 0.5$ mm) due to the absence of rotational velocity component of velocity at the center and no the slip-boundary condition at the wall, respectively. Similarly, radial velocity

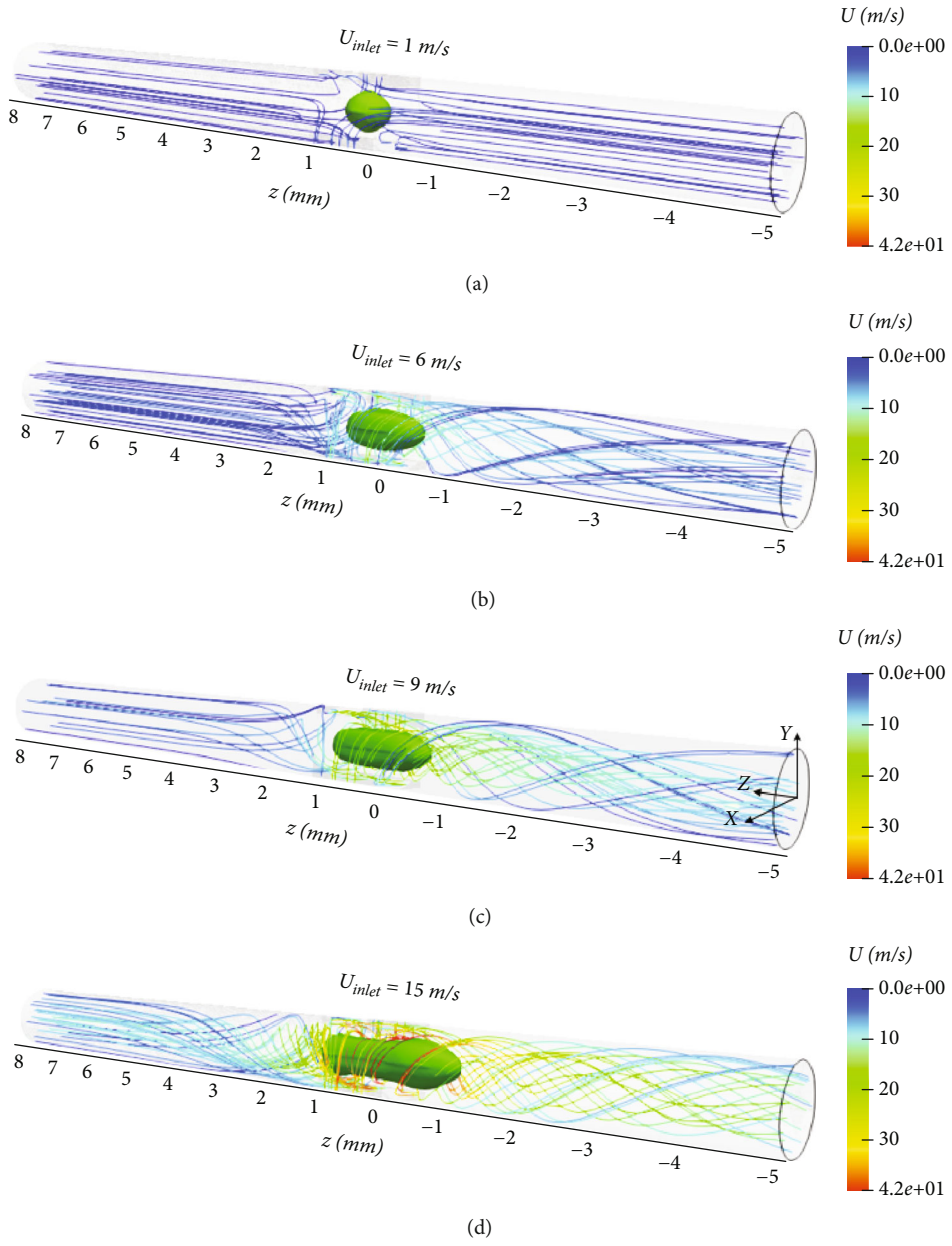

FIGURE 4: Three-dimensional isosurfaces of OH mass fraction at $\phi = 0.5$ along with the stream tubes at (a) $U_{\text{inlet}} = 1$ m/s; (b) $U_{\text{inlet}} = 6$ m/s; (c) $U_{\text{inlet}} = 9$ m/s, (d) $U_{\text{inlet}} = 15$ m/s. Iso-surfaces of OH illustrated for (a) $Y_{OH} = 10^{-3}$, (b) $Y_{OH} = 4.2 \times 10^{-3}$, and (c, d) $Y_{OH} = 5 \times 10^{-3}$.

is zero at the center ($X = 0$) and the wall ($X = 0.5$ mm) due to the axisymmetric shape of the flame and no-slip boundary condition, respectively. As the distance from both the center and the wall increases, the circumferential velocity rises.

At the inlet velocity of 1 m/s, circumferential velocity values are one order lower compared to the range of 6 m/s to 15 m/s, confirming minimal circulation of the stream tubes at the inlet velocity of 1 m/s compared to the inlet velocity range of 6 m/s to 15 m/s. This observation also corroborates the absence of tubular flame formation at the inlet velocity of 1 m/s.

According to Figures 5(b) and 5(d), The circumferential velocity experiences an increase near the wall as the inlet velocity rises. Furthermore, the velocity gradient sharply rises near the wall within the inlet velocity range of 9 m/s to 15 m/s. Consequently, there is a reduction in flow residence time near the wall and an enhancement of centrifugal forces. Since centrifugal acceleration is directly proportional to the second power of the circumferential velocity and inversely proportional to the tube radius as $a = (u_\theta)^2/r$, the centrifugal force is more robust at $U_{\text{inlet}} = 15$ m/s due to the lower radius and enhanced circumferential velocity. Consequently, the stratification effect is expected to become more significant with increased inlet velocity, as the centrifugal forces act to stratify the burned and unburned gases [44]. This enhances the flame's aerodynamic stability and smoothness in accordance with the Rayleigh stability criterion. Comparing Figures 5(a) and 5(c), it is observed that

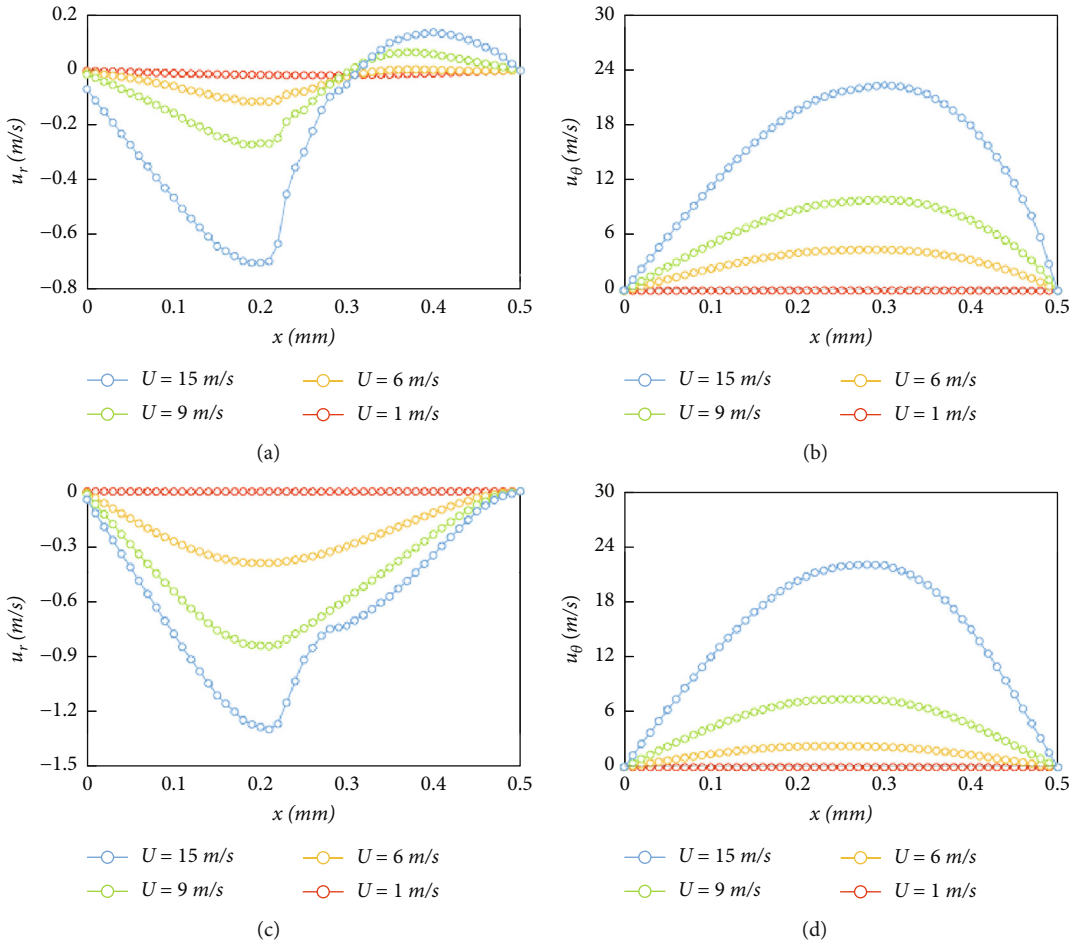

FIGURE 5: Circumferential (u_θ) and radial velocity (u_r) variations along the radial distance at equivalence ratio of 0.5 on the cross-sections located at (a, b) $Z = -1$ mm and (c, d) $Z = 1.5$ mm.

the radial velocity values are one order lower than those of the circumferential velocity, consistent with the experimental findings of Shimokuri et al. [48] for 3.6 mm diameter microtubes.

The radial velocity increases with the inlet velocity; however, the maximum radial velocity values in the flow field remain one order lower than the inlet velocity. This characteristic is another advantage of tubular flames, as it contributes to a higher upper flammability limit compared to cases where the combustible mixture is axially injected. According to Figure 5(a), the direction of the radial velocity shifts from the center towards the wall, with negative and positive values separating at $X = 0.3$ mm. This a result of stronger centrifugal forces induced by the swirling flow effects on the shorter side, which causes the stream tubes to tilt further. Since the reactive flow distance is from the inlet towards the outlet, centrifugal forces bifurcate the u_r by directing the reactive flow towards the wall. This leads to flame tip expansion, as depicted in Figure 4(d), where the flame tip expansion is more visible at $U_{\text{inlet}} = 15$ m/s because of the enhanced u_r.

Diagram of temperature variations along the radial direction on the cross-section at $Z = 0.5$ mm is presented in Figure 6(a) for various inlet velocities at an equivalence ratio of 0.5. Analysis of the diagram reveals that the maximum temperature is consistently located at the center of the microtube cross-section ($X = 0$) for all inlet velocities, with the temperature decreasing to the wall temperature at $X = 0.5$ mm (where fixed at 960 K). The nonuniformity in the temperature gradient increases with the inlet velocity, with the maximum nonuniformity observed at the inlet velocity of 15 m/s. Additionally, the maximum temperature difference between the center and the wall is achieved at the inlet velocity of 15 m/s. At $U_{\text{inlet}} = 1$ m/s, the temperature gradient appears more uniform compared to others because the circumferential velocity is so low that the centrifugal forces cannot well stratify the flow. Also, the radial velocity value is relatively weak and cannot stand up to the burning velocity, according to Figures 5(a) and 5(c). Regarding Figure 6(a), the temperature gradient increases near the wall for the inlet velocities in the range of 1 m/s to 6 m/s. This is attributed to the enhancement of burning velocity due to temperature increase in the flame kernel, dominating over the enhancements in radial and circumferential velocity, thus maintaining the flame front closer to the wall and increasing heat loss. Conversely, the temperature gradient decreases near the wall as the inlet velocity increases up to

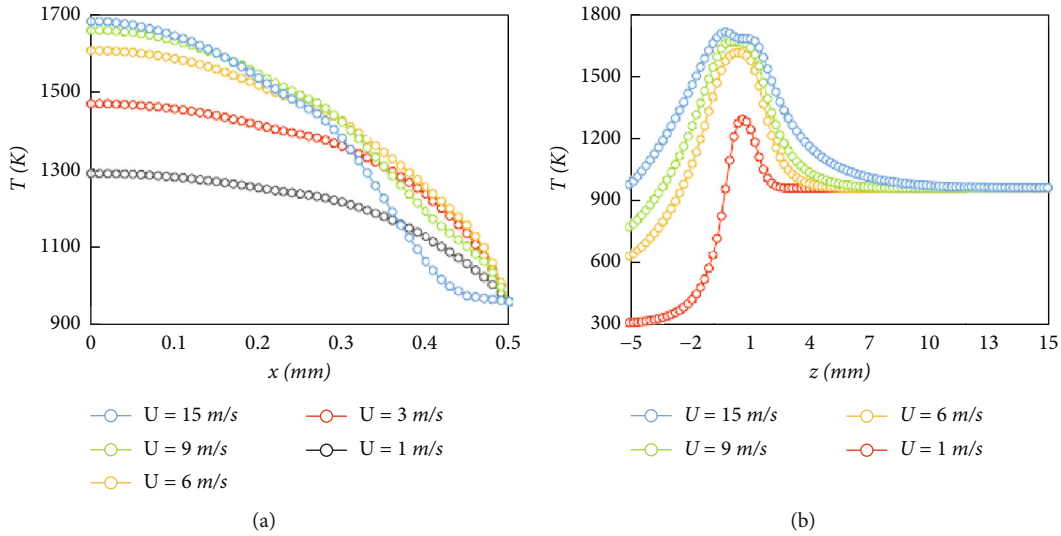

FIGURE 6: Temperature variations with the inlet velocity at equivalence ratio of 0.5 on the cross-section located (a) at the position $Z = 0.5$ mm and (b) along the microtube centerline.

9 m/s, as the inlet velocity enhancement outweighs the burning velocity enhancement. Finally, the flow becomes completely stratified, and the temperature gradient nearly decreases to zero. Consequently, zero heat loss to the wall resulted. In other words, the high circumferential velocity reduces the radial thermal diffusion time scale near the wall, causing the slope of the temperature profile to drop to zero and minimizing heat loss.

Therefore, the released heat of combustion accumulates in the center of the microtube, and it causes an increase in the temperature of the center of the microtube. Additionally, the flame shrinkage observed at the inlet velocity of 15 m/s (Figure 6(a)) can be attributed to the intensified bifurcation and stratification effects of radial velocity, as depicted in Figures 5(a) and 5(c). The maximum temperature at $U_{\text{inlet}} = 9$ m/s is close to the maximum temperature at the $U_{\text{inlet}} = 15$ m/s. Despite the negligible temperature gradient near the wall at $U_{\text{inlet}} = 9$ m/s, the temperature gradient at $U_{\text{inlet}} = 9$ m/s contributes to preheating of the inlet mixture. Interestingly, the preheating effect at $U_{\text{inlet}} = 9$ m/s appears to be more optimized because it compensates the existence of a temperature gradient near the wall despite its lower velocity. Moreover, the maximum temperature at $U_{\text{inlet}} = 15$ m/s is just 24 K higher than that at $U_{\text{inlet}} = 9$ m/s.

Diagram of gas-phase temperature variations along the axis of the microtube is depicted in Figure 6(b). According to the diagram, they are more pronounced on the short side due to the enhancement of inlet velocity, leading to an increase in the maximum temperature. Despite the longer length and the presence of the heated wall on the long side, the gas-phase temperature is primarily controlled by the wall temperature. With the enhancement of inlet velocity, the region where the gas-phase temperature exceeds the wall temperature extends. Due to the perpendicular flame elongation, the heat release rate increases with the inlet velocity. Also, the released heat of combustion accumulates in the center, leading to temperature growth on the axis due to the reduction of the temperature gradient near the wall at inlet velocities higher than 9 m/s. Finally, the accumulated heat of combustion transfers to the outlets through the microtube centerline via flow velocity. Higher inlet velocity results in higher flow velocity, leading to the spread of the high-temperature zone along the axis.

3.2. Investigation of the Flame Characteristics under the Stimulated Inlet Condition

3.2.1. Flame Propagation Modes. This section presents a detailed investigation into the periodic behavior of the flame under inlet excitations with a focus on the variations of the exciting amplitude from hydrodynamic and kinetics perspectives. Flame responses were obtained for exciting amplitudes ranging from 0.2 to 1 at an average inlet velocity of 9 m/s, forcing frequency of 1000 Hz, and equivalence ratio of 0.5. The flame response frequency was determined as for all cases. Consequently, the time interval from $t = 6.9$ ms to $t = 7.9$ ms was chosen as a cycle of the periodic evolutions. With this regard, the time $t = 6.9$ ms set as the beginning of the cycle. Also, the time of $t = 7.9$ ms set as the last time of the cycle and the beginning time of the next cycle. Two propagation modes, namely, flame with semirepetitive extinction/ignition (FSREI) and pulsating flame, were observed as the exciting amplitude varied from 0.2 to 1. The pulsating mode was predominant at the exciting amplitudes of 0.2 to 0.6, while the FSREI mode emerged at the exciting amplitude of 1. Further details on these modes are elaborated and discussed in the subsequent sections.

(1) Flame with Semirepetitive Extinction/Ignition (FSREI). Before going into details, it is worth noting that during the propagation, the flame with repetitive extinction/ignition (FREI) typically undergoes five phases during a cycle: initiation phase, ignition phase, propagation phase, weak reaction phase, and flowing phase [6, 7, 25]. Given the similarity of

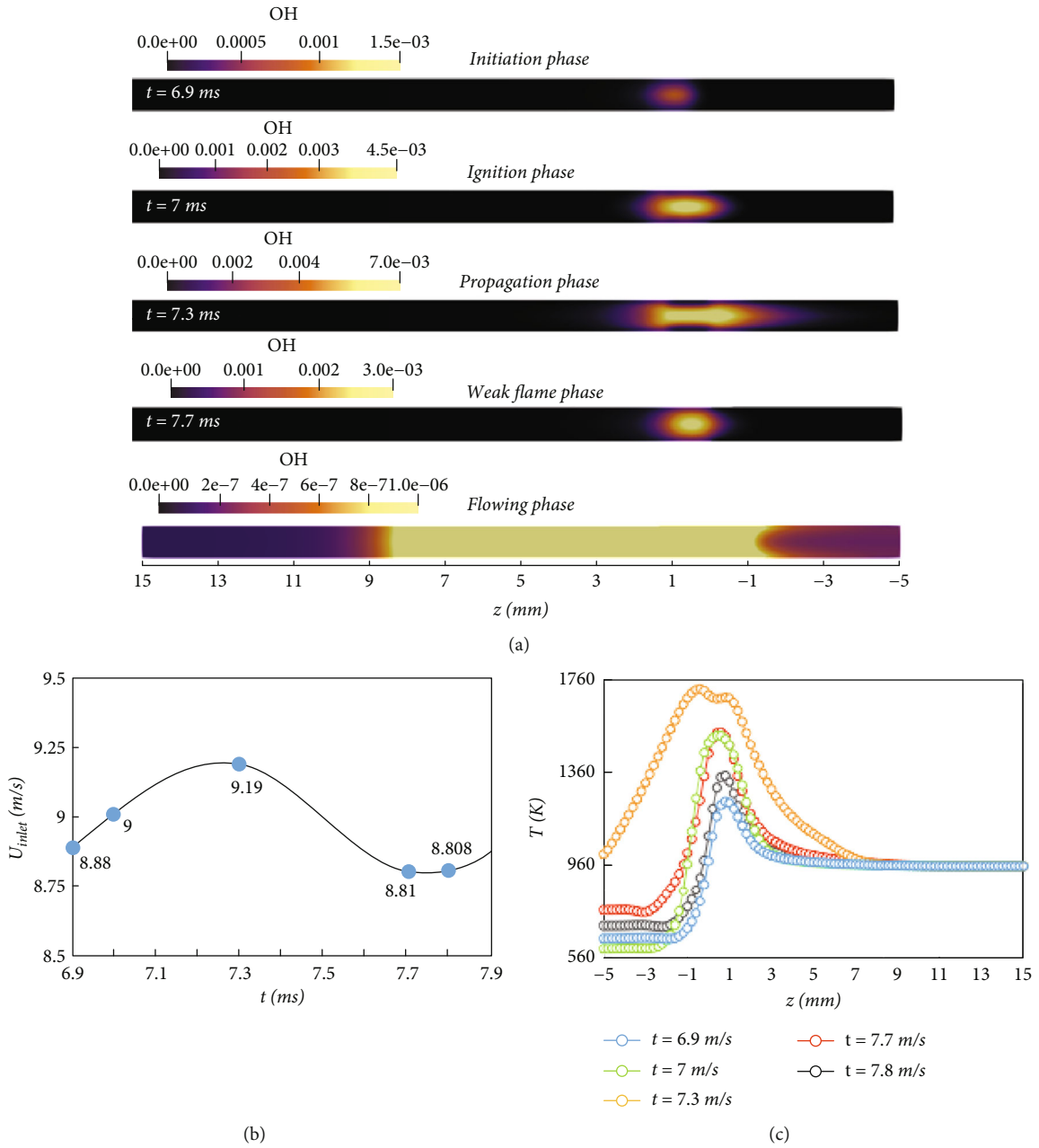

FIGURE 7: (a) Evolution of OH mass fraction contours during a cycle in the FSREI mode (U_{inlet} = 9 m/s, F = 1000 Hz and A = 1); (b) the diagram illustrating the evolution of inlet velocity during a cycle, and (c) the temporal variation of temperature along the axis of microtube during a cycle.

the flame propagation mode at the exciting amplitude of 1 to the FREI mode, the term "FSREI" (flame with semirepetitive extinction/ignition) is used to classify this mode. However, there may be differences with them. In the FREI, the flame completely extinguishes, and the flow temperature does not exceed the wall temperature at the initiation and the flowing phases [7, 25]. In contrast, in the present study, the flame does not fully extinguish, as the temperature of the flame kernel remains higher than the wall temperature during the initiation and flowing phases. This distinction led to the adoption of the term "FSREI" to highlight the differences while maintaining analogies to the FREI mode.

Figure 7 presents a comprehensive analysis of the FSREI phenomenon by showing the contours of OH mass fraction variations during a cycle (a), the temporal evolution of the inlet velocity during a cycle (b), and the temporal evolution of the gas-phase temperature along the axis of the microtube (c). These results are obtained under the operating conditions of U_{inlet} = 9 m/s, F = 1000 Hz, A = 1, and ϕ = 0.5. Contours of OH have been classified into five phases: initiation, ignition, propagation, weak flame phase, and flowing phase, with respective instances assigned above the contours. Legends of the contours are chosen distinctively to ensure proper distinction between phases. The temporal evolution

of the inlet velocity is depicted for the current cycle, with maximum and minimum values of 9.192 m/s and 8.808 m/s, respectively. Additionally, values corresponding to the propagation phases are marked and highlighted in the diagram. The temperature evolution graphs in Figure 7(c) are categorized based on instances corresponding to the phases of FSREI. The initiation phase occurs at the instance t = 6.9 ms. During this phase, the flame exhibits an almost elliptical shape (Figure 7(a)) and reaches its lowest temperature during the cycle (Figure 7(c)). The inlet velocity is U_{inlet} = 8.879 m/s, and its diagram shows a positive slope at the instance of t = 6.9 ms (Figure 7(b)). Therefore, the mass flow rate increases by inlet velocity enhancement until the next phase. According to Figure 7(c), the gas-phase temperature is primarily governed by the wall temperature on most of the long side, while the short side exhibits a higher temperature gradient along the centerline. Consequently, the heat transfer rate from the flame in the axial direction is higher on the short side.

As the inlet velocity increases up to 9 m/s at t = 7 ms, the flame exhibits increased robustness due to enhancement in OH mass fraction. Additionally, the flame expands in the axial direction, and its kernel becomes more elliptical because flame fronts instantly propagate towards both short and long sides. The peak point temperature increases in the temperature diagram and shifts towards the short side. Moreover, the gas-phase temperature exceeds the wall temperature on the long side to a greater extent compared to the previous moment. However, the majority of the long side's length is still influenced by the wall temperature. Despite the higher inlet velocity resulting in higher flame temperature, the outlet temperature decreases on the short side due to an increased temperature gradient. After ignition, the flame enters to the propagation phase at t = 7.3 ms, exhibiting its strongest mode corresponding to the maximum inlet velocity (U_{inlet} = 9.19 m/s). Consequently, fresh inlet mixture feeds the flame adequately, so the maximum temperature during the cycle is obtained (Figure 7(c)). The gas-phase temperature completely exceeds the wall temperature on the short side and does so over a larger area on the long side. The peak point bifurcates, with one moving downstream on the short side and the other appearing on the long side lower than that one on the short side. This divergence occurs because the flame elongation on the short side is greater than that on the long side, resulting in higher temperatures on the short side. Tubular flame is completely formed at this time. During the transition of the flame from the initiation to the ignition phase, the increase in temperature gradient along the centerline leads to a higher rate of heat transfer to the flame tips. Consequently, the temperature of the flame tip increases during the propagation phase, leading to a bifurcation in the temperature diagram. Additionally, due to differences in temperature gradients, the rise in temperatures at the flame tips is unequal for both sides. The short side experiences greater temperature enhancement due to its higher temperature gradient compared to the long side.

The slope of the inlet velocity diagram begins to decrease after the instance of t = 7.3 ms. With a lower mass flow rate, the feeding of the flame from the fresh mixture is reduced, resulting in a decrease in flame temperature. Consequently, the peak point attributed to the long side disappears, and the one attributed to the short side moves back to its previous position as the flame weakens and shrinks towards its kernel. This leads to an increase in the centerline temperature gradient again on the short side, while the gas-phase temperature tends towards the wall temperature on most of the long side. The inlet velocity reaches its lowest value from t = 7.7 ms to t = 7.8 ms. Consequently, the weakening of the flame continues until the instance t = 7.8 ms at which the flame enters the flowing phase. In the flowing phase, the flame front on the short side is concave towards the products, while it is almost flat towards the products on the long side. During this phase, the remaining H_2 and O_2 from the previous phases react together. However, since most of H_2 and O_2 have been consumed during the previous phases, lower heat is released, leading to a decrease in flow temperature in the flowing phase. As the inlet velocity increases again in the next cycle, the fresh mixture feeds the flame with additional fuel. The heat released in the previous phase ignites the fresh mixture in the initiation phase, preventing the flame from extinguishing. Increasing the mass flow rate of the fresh mixture reduces the excessive time lag between feeding the flame and the heat released in the previous phase. Consequently, the flame is not extinguished during the interval between the flowing and initiation phases.

Figure 8 provides a detailed illustration of the FSREI mode, focusing on changes in the flame front during the cycle. OH iso-level surfaces are illustrated in the vicinity of the stream tubes, with the legend of the stream tubes arranged according to hydrodynamic pressure. Additionally, velocity vectors are provided to indicate the presence of negative propagation speed. Furthermore, Figure 9 plots the axial flow velocity component (u_Z) over the axis of the microtube during the cycle. To enhance clarity and visibility of velocity vectors and stream tubes beside the flame, the velocity vectors are not scaled, and the results are illustrated for a portion of the microtube clipped from the short side outlet to the position of Z = 5 mm. In other words, the short side is completely shown, and the long side is shown up to 5 mm from the beginning of the slots (Z = 0).

According to Figure 8(a), flow velocity vectors are codirectional on the long side and all points downstream. Accordingly, the stream tubes are parallel, indicating the absence of circulation or recirculation zones on the long side. In contrast, on the short side, the velocity vectors are not parallel on the short side, and they are angled in various directions. Some vectors are directed inward the channel, while others are outward the channel. Additionally, some vectors entirely exhibit rotational motion in front of the flame on the short side. As a result, the stream tubes are curled and tilted in front of the flame on the short side, where the deviation angles of the vectors are increased. This phenomenon occurs due to the collision of two countercurrents: one flowing from the flame towards the downstream of the short side, and the other flowing from the outlet of the short side towards the channel inside. The backflow from the previous moments contributes to this effect. The position of the recirculation kernel can be precisely determined using the diagram in Figure 9.

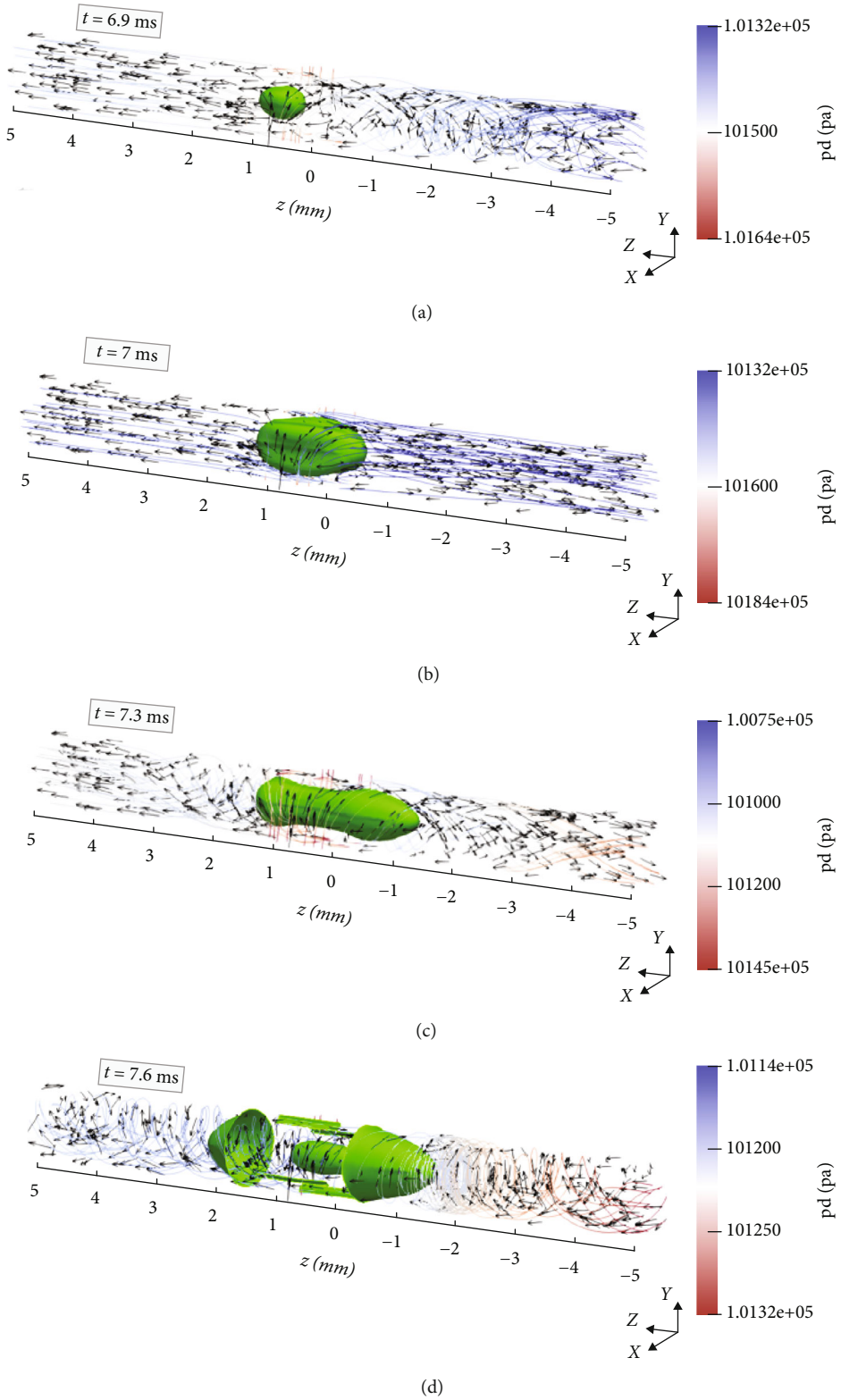

Figure 8: Continued.

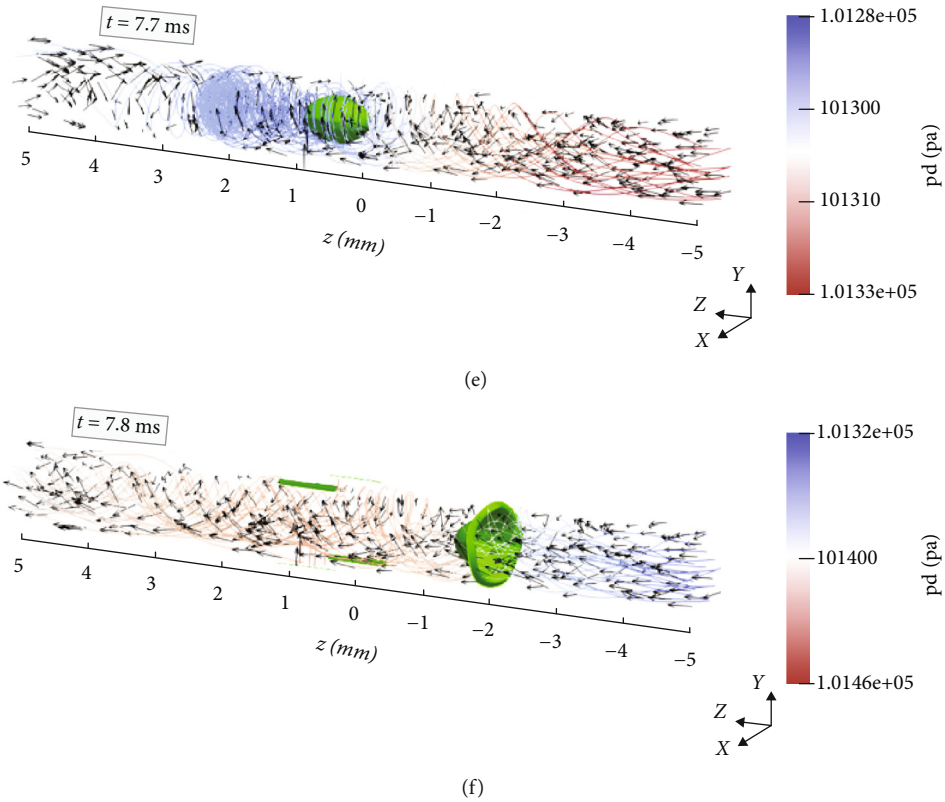

FIGURE 8: FSREI propagation mode during a cycle at $U_{\text{inlet}} = 9$ m/s, $\phi = 0.5$, $A = 1$, and $F = 1000$ Hz with three-dimensional isosurfaces of OH mass fraction (Y_{OH}), flow velocity vectors, and stream tubes. Isosurfaces of OH illustrated for (a) $Y_{OH} = 6 \times 10^{-4}$, (b) $Y_{OH} = 25 \times 10^{-4}$, (c) $Y_{OH} = 5 \times 10^{-3}$, (d) $Y_{OH} = 5 \times 10^{-3}$ and $Y_{OH} = 5 \times 10^{-4}$, (e) $Y_{OH} = 25 \times 10^{-4}$, and (f) $Y_{OH} = 7 \times 10^{-7}$.

The point where the graph intersects the z-axis corresponds to the desired position. According to the figure, the backflow enters the short side at the axial velocity of 6 m/s and penetrates to a considerable distance along the axis inside the microtube at $t = 6.9$ ms. The axial velocity becomes zero at position $Z = -1.4$ mm. Therefore, the recirculation zone generates there, in front of the flame (Figure 8(a)).

The axial velocity is nearly negligible on the long side, according to Figure 9. In addition, the parallel stream tubes on the long side imply that the rotational velocity can be disregarded. Flow velocity on the long side is much lower than on the short side in this phase. As depicted in Figure 8(a), hydrodynamic pressure increases around the flame near the slots and gradually decreases until the middle of the short side's length, where it reaches the ambient pressure. The recirculation zone dissipates as the flame progresses past the initiation phase. At this moment, velocity vectors are not deviated except around the flame, where the incoming flow enters circumferentially. Consequently, stream tubes become parallel on both sides (Figure 8(b)). Figure 9 further confirms the absence of backflow on the short side. Additionally, flow velocity significantly increases due to the increment in inlet velocity.

Rotational velocity intensifies around the flame during the propagation phase (Figure 8(c)). Velocity vectors exhibit angles around and in front of the flame; consequently, the stream tubes have been tilted in front of the flame on both sides. However, the angle of deviation decreases, and the stream tubes become parallel as the flow moves away from the flame towards the downstream. Axial flow velocity increases on both sides and reaches its maximum value during the cycle, according to Figure 9. The axial velocity experiences a sharp decrease from $Z = 0$ to $Z = -1$ mm due to the increment in rotational velocity at the flame tip. Subsequently, the axial velocity increases towards the short side outlet, where the stream tubes become parallel, and the rotational velocity decreases.

According to Figures 8(a) and 8(d), separation appears in the flame kernel and tip. Due to the inlet velocity decrease, fewer mass flow rate is entered into the flame kernel. This effect leads to a burning velocity decrease in the flame kernel instantly. At the same time, the flame tips have a higher burning velocity than the previous instance. Consequently, the flame tip burns faster than the kernel, which causes the separation of the flame kernel and tips. The main kernel of the flame remains near the inlet, where the combustible mixture enters through the slots. At the same time, separated tips accelerate to the outlets.

It is evident that a significant circulation zone is generated in front of the flame tip on the short side, as a result of interactions between the main flow and negative propagation speed. The backflow consists of products and even unburned fuel/oxidizer from the previous instances, which obstructs the main flow. Simultaneously, a substantial vertex is generated and the rotating flow intensifies as the main flow must divert the backflow to satisfy the mass conservation. Consequently, the

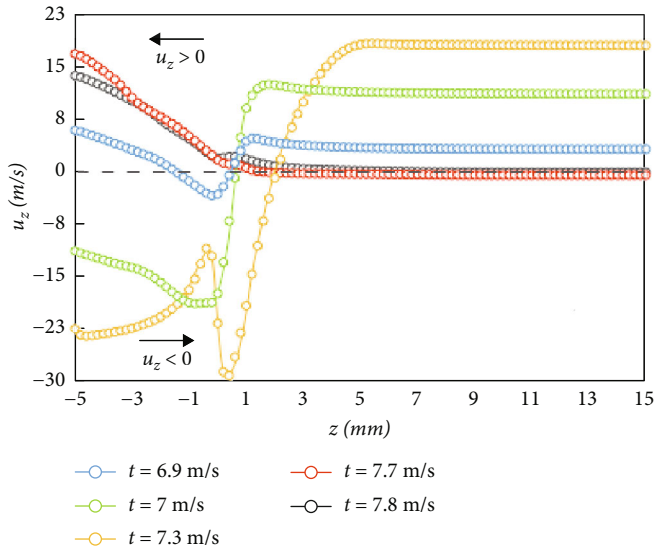

FIGURE 9: Temporal variation of the axial flow velocity component (u_Z) along the z-axis during a cycle of the FSREI; $U_{\text{inlet}} = 9$ m/s, $\phi = 0.5$, $A = 1$ and $F = 1000$ Hz.

main flow becomes completely rotating. This effect causes the flame tip to expand towards the wall, where the separated flame tip eventually extinguishes due to the imbalance between the heat release rate and heat loss rate (Figure 8(e)).

As the inlet velocity continues to decrease at instance $t = 7.7$ ms, the negative propagation speed intensifies, pushing the massive circulation zone to the long side. Local pressure reduces in the circulation zone below ambient pressure, inducing backflow in the long and short sides. The backflow is more considerable on the short side (Figure 9) due to the significant pressure gradient. In contrast, the backflow on the long side is local and not comparable to that on the short side. For instance $t = 7.8$ ms, pressure increases near the slots (where the main flow enters) and on the long side due to the mixing of backflow with the incoming main flow. Consequently, the main flow finds its way through the long side to maintain mass conservation. This results in an enhancement of axial flow velocity on the long side. However, axial flow velocity decreases with a gentle slope towards the outlet due to the longer length (Figure 9). The evolution of inlet velocity depicted in Figures 8 and 9 leads to fluctuations in heat release rate, especially on the short side where the flame elongation is more significant. These fluctuations in heat release rate cause fluctuations in temperature and density fields, thereby affecting the pressure field and leading to the creation of backflow.

Moreover, the weakening of the flame after the propagation phase is attributed to the separation of the flame tips from its kernel due to differences in burning speed. In addition, the backflow in the flowing phase is forceful enough to prevent dissipation of the released heat from previous phases. Therefore, unlike the FREI mode, the flame is not extinguished and immediately enters the initiation phase.

Reaction rate evolution related to fast reactions has been shown in different FSREI phases along the centerline in Figure 10. Additionally, Figure 11 illustrates the temporal variations of mass fractions of species along the centerline of the microtube during a cycle of FSREI. At the initiation phase, the reaction rate of R3 significantly surpasses that of other reactions in Figure 10. This is attributed to the abundance of fresh premixed H_2/air surrounding the flame front, and the mass fraction of H_2 is at the highest level at the inlet according to Figure 11. The incoming fuel (H_2) reacts with OH radicals in R3 and produces H_2O and H. Due to the H production, reactions R1, R11, and R9 are activated simultaneously, where H radicals are consumed. The produced HO_2 in R9 consumes in R11 ($HO_2 + H = OH + OH$), leading to the production of OH radicals. Additionally, the produced H in the R3 activates R1 resulting in the production of more OH radicals. As illustrated in Figure 11, the mass fraction of heavier species containing H_2O, HO_2, and H_2O_2 reaches its maximum value during the initiation phase of the cycle, whereas the radical species containing H, O, and OH reach their minimum value. In other words, elementary reactions progress towards the production of heavier species during the initiation phase.

Flame temperature increases in the ignition phase according to Figure 7(c). Consequently, the reaction rates of R1 and R2 increase due to temperature enhancement and lead to producing more H and OH radicals. In other words, the H and OH production rate increases in the R1 and R2. Simultaneously, R11 becomes more active due to the increment in H concentration, which produces more OH. Additionally, the rate of R8 increases, where H and OH react and produce water. It has been proven in Figure 11 that the production rate of H, OH, and O are increased during the ignition phase because H, OH, and O experienced a sharp increase in their mass fraction. On the other hand, the mass fraction of the H_2O, HO_2, and H_2O_2 decreases around the position $Z = 0$, where the flame center is placed. According to Figure 11, mass fraction variations of the H_2O exhibit two peaks around the positions of $Z = 3$ mm and $Z = -1$ mm indicating that more complete reactions occur at those points [6]. Conversely, a minimum

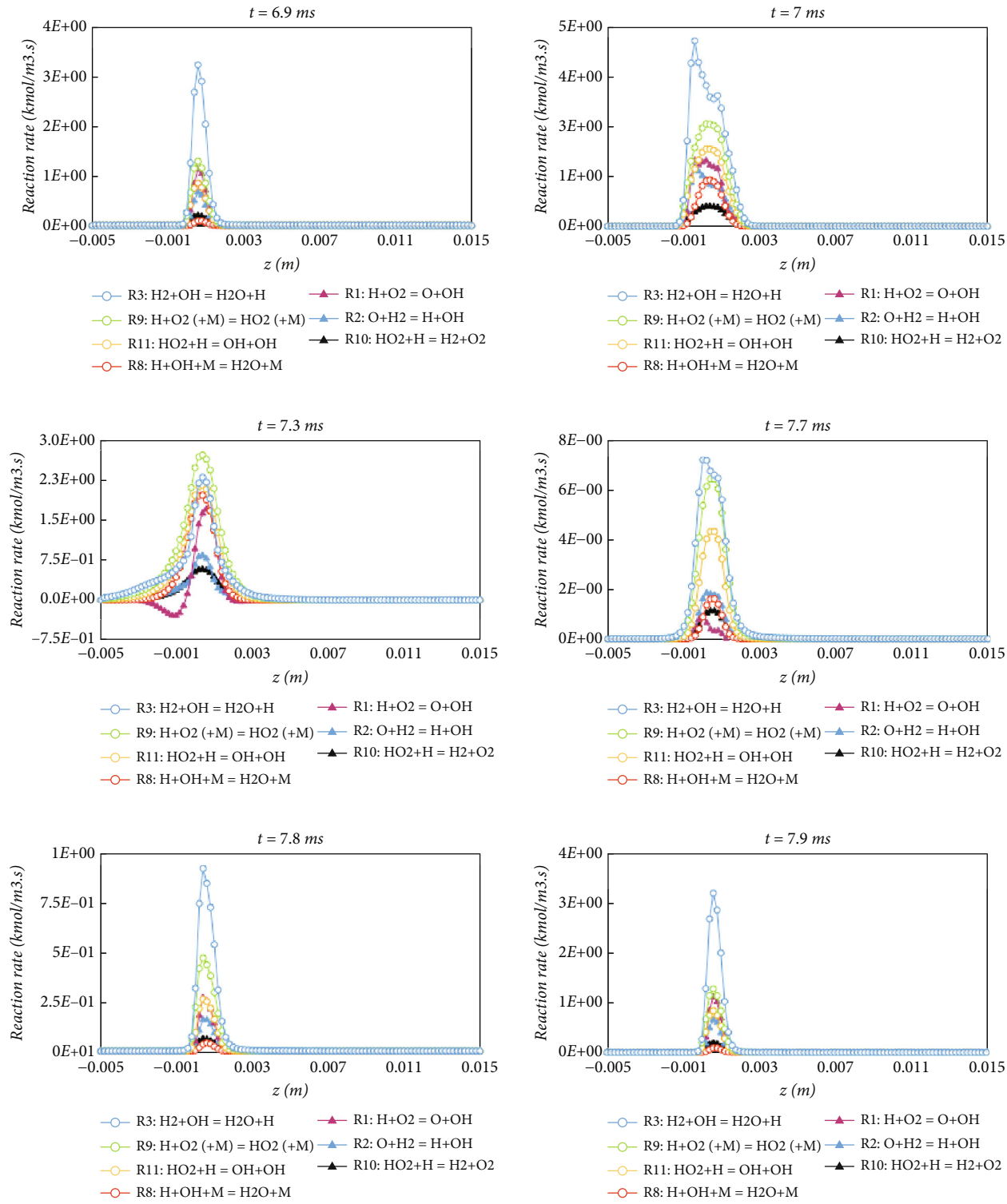

FIGURE 10: Temporal variation of reaction rates along the centerline during a cycle of the FSREI; $U_{inlet} = 9$ m/s, $\phi = 0.5$, $A = 1$ and $F = 1000$ Hz.

point is observed between them suggesting that more incomplete reactions occur, where the peak points of the radical diagrams are located. This is in accordance with the R3 reaction rate variations in Figure 10, which exhibits two peak points near those positions. Notably, the peak point near the $Z = -1$ mm is higher than the other peak point near the $Z = 3$ mm. Consequently, the H_2O production rate increases near the $Z = -1$ mm, so the peak point of H_2O mass fraction variations diagram near the $Z = -1$ mm has a higher value.

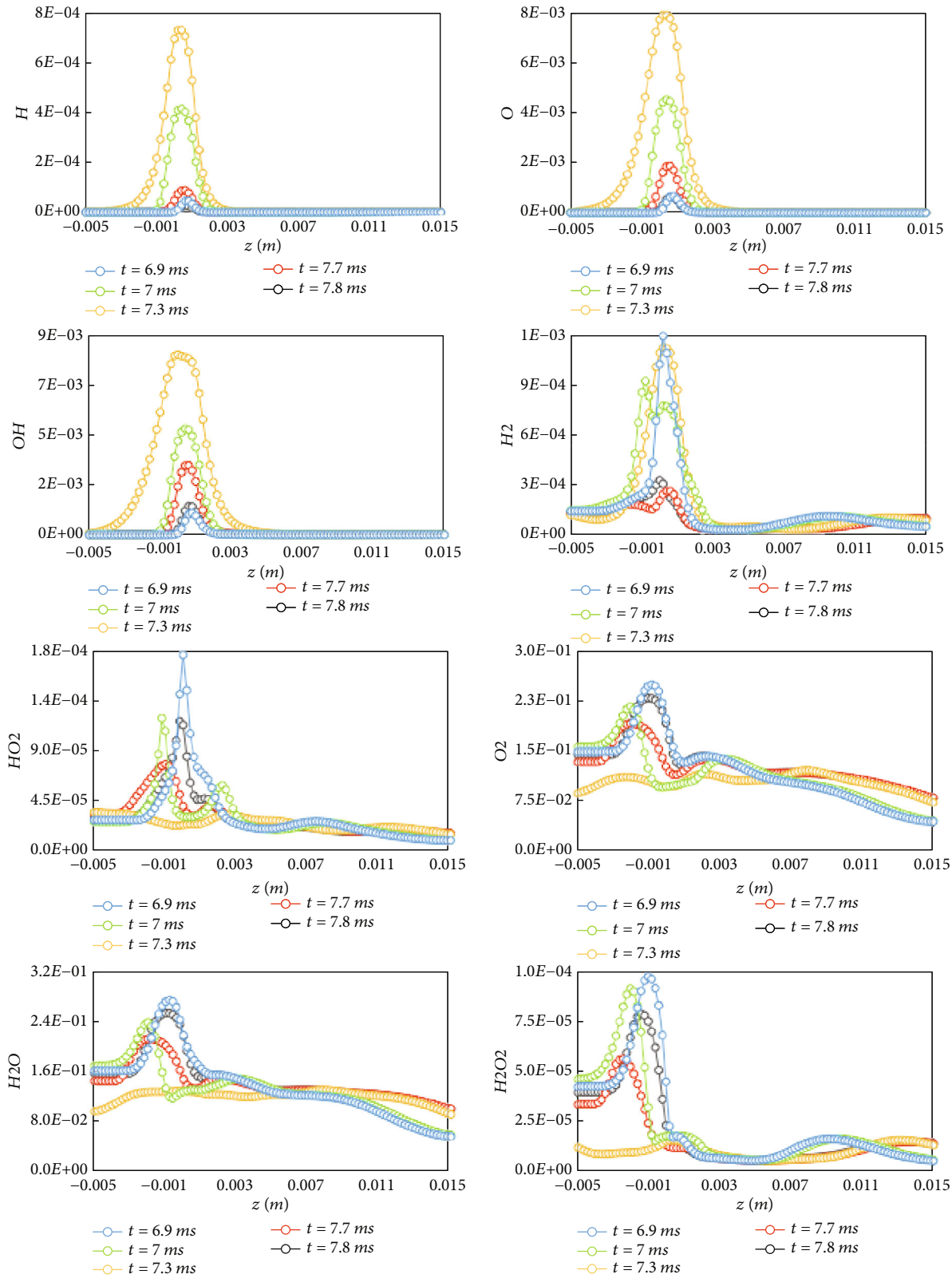

Figure 11: Temporal evolution of the species along the centerline during a cycle of the FSREI; $U_{inlet} = 9$ m/s, $\phi = 0.5$, $A = 1$ and $F = 1000$ Hz.

During the propagation phase, radicals reach their maximum value in the cycle, while heavier species exhibit their minimum value. Also, H_2O, HO_2, and H_2O_2 variations along the centerline are more monotonous. It can be inferred that the production rates of H_2O and HO_2 decrease due to the reduced reaction rates of R3 and R9. Despite the

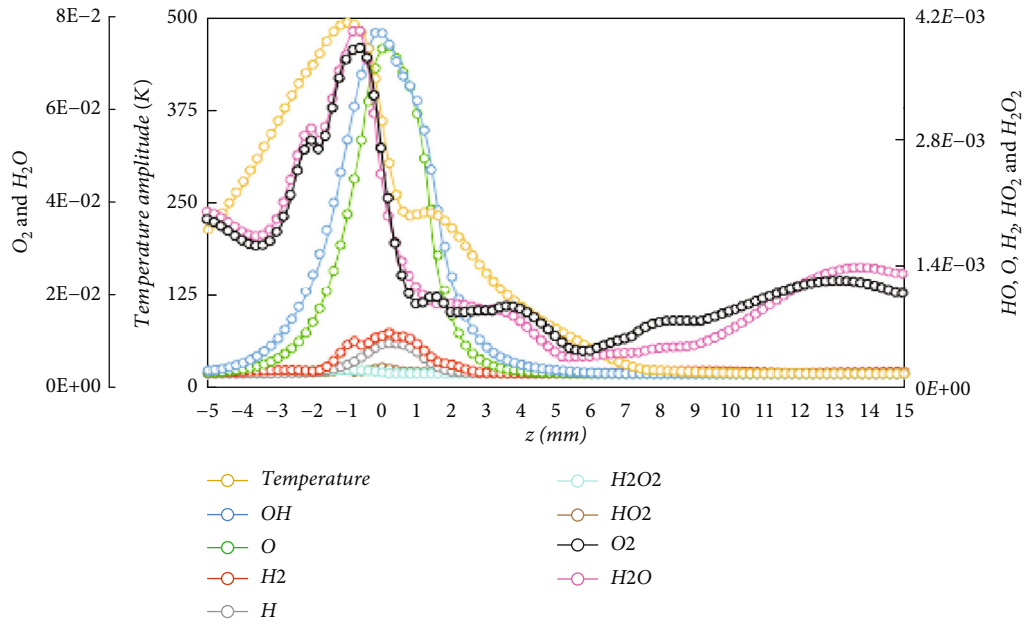

FIGURE 12: Variations of the response amplitudes of species mass fractions and gas-phase temperature along the microtube axis of FSREI; $U_{inlet} = 9$ m/s, $\phi = 0.5$, $A = 1$ and $F = 1000$ Hz.

increased reaction rate of R8 increases, the enhancement in the H_2O production rate in R8 is insufficient to compensate for its reduction in R3, so the net production rate of the H_2O decreases. About the HO_2, the reaction rate of the R9 decreases, which mining that the production rate of HO_2 decreases. Also, the reaction rate of the R11 increases, meaning that the consumption rate of HO_2 increases. Therefore, the net production rate of HO_2 decreases. Although H2 participates in both R2 and R3 reactions, the reaction rate of R3 surpasses that of R2, suggesting a higher tendency for H2 to react with OH rather than O. This is attributed to the higher preexponential factor and lower activation energy of R3, as indicated in Table 1. Consequently, the reaction rate of R3 remains elevated than R2 throughout all phases. The rate of all reactions decreases in the weak flame phase because the temperature decreases, according to the Figure 7(c). Radicals experience a significant decline in their production rate during the cycle because the mass fractions of H, O, and OH have the sharpest decline, as shown in Figure 11. Additionally, the lowest level of H2 mass fraction contributes to a reduction in the rate of R2, leading to decreased production rates of H and OH in R2. Consequently, the production rate of H and OH decreases in R2. Therefore, the rate of R3 experiences a sharp decrease due to the diminished OH concentration, while the reaction rate of R1 exhibits a notable decline compared to the previous phase due to reduced production rates of H and OH. Therefore, the rate of R8 sharply decreases due to the shortage of reactants H and OH.

The gas-phase temperature drops again in the flowing phase, as depicted in Figure 7(c). Consequently, the production rates of H, O, and OH decrease, while the production rates of H_2O, HO_2, and H_2O_2 increase. Finally, at the time of $t = 7.9$ ms, the cycle ends, and later cycle begins in the initiation phase. According to Figure 10, reaction rate diagrams exhibit complete similarity at instances of $t = 6.9$ ms and $t = 7.9$ ms.

Figure 12 illustrates the variations in response amplitudes of species mass fractions along the axis of the microtube. Due to the difference in the order of the magnitudes, results are presented in a double-axis chart. Results belonging to O_2 and H_2O exhibit the same order of magnitude, larger than others by one order; hence, their variations are displayed on the left axis. The results belonging to OH, O, H, H_2, H_2O_2, and HO_2 are illustrated on the right axis. In addition, the range of variations of the results belonging to the temperature is illustrated on the left axis alongside O_2 and H_2O. Response amplitudes are determined by responses to the inlet excitation of $A = 1$. Near the slots, gas-phase temperature and all species peak have their maximum values for the response amplitudes due to proximity to the applied inlet. Moving away from the slots reduces the effect of the inlet excitations on the response amplitudes. Variation of the response amplitude is linear for the temperature on the short side, while it is nonlinear and has a greater slope on the long side. Its value reaches zero at the position $Z = 5$ mm. As a result, from this area onwards there are no temperature fluctuations. Response amplitudes of H_2O_2, HO_2, H, and H_2 are minimal compared to other species, especially far from the slots. Species including OH, O, H_2O, and O_2, however, respond more sensitively to the inlet excitations. Fluctuations of OH and O are damped on the both sides of the microtube, but fluctuations of H_2O and O_2 survive upon the outlets on the both sides. As a result, impacts of the inlet excitations are observed in the outlets only for H_2O and O_2 in the FSREI mode.

(2) Pulsating Flame. As the exciting amplitude drops to 0.6 and 0.2, the flame responds, and its propagation mode

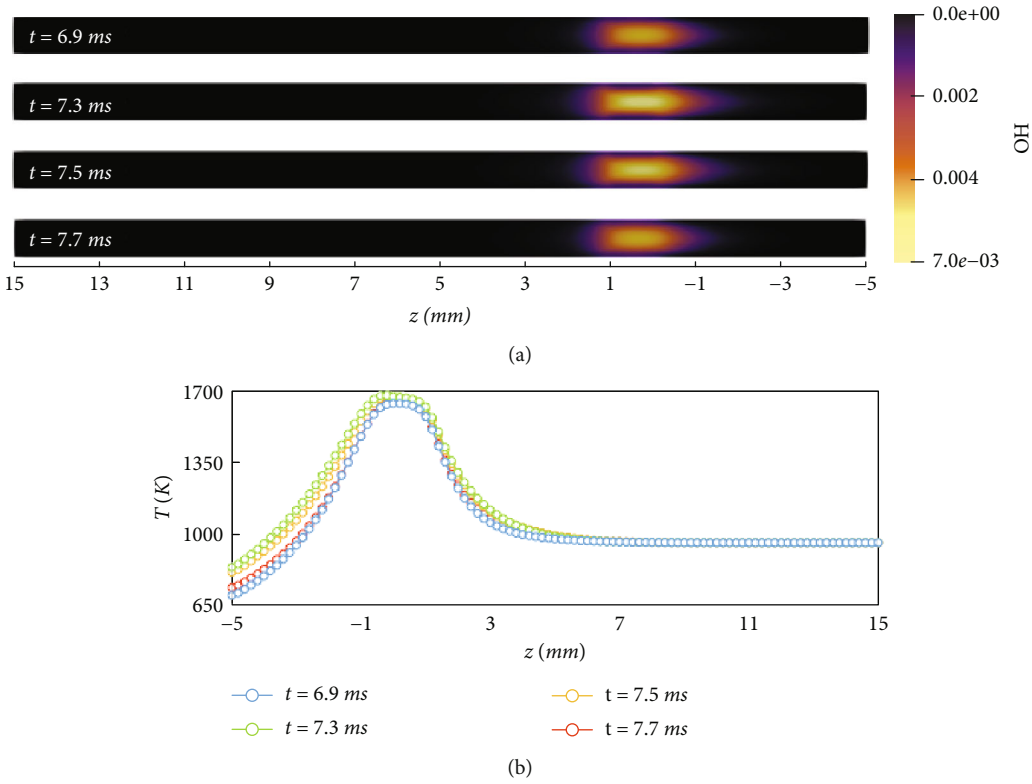

FIGURE 13: (a) Contours of OH mass fraction evolution and (b) temporal variations of the gas-phase temperature on the centerline of the microtube during the cycle in the pulsating flame mode ($U_{\text{inlet}} = 9$ m/s, $F = 1000$ Hz and $A = 0.2$).

changes to the pulsating mode. In the pulsating mode, the flame does not reach the near-extinguishing conditions and weak flame phase. It just expands and shrinks around a fixed position. Flame response at the exciting amplitude of 0.2 has been elected to be discussed in this section. The flame is less impacted by the inlet excitations than the FSREI, at the exciting amplitude of 0.2.

Contours of OH mass fraction have been illustrated during a cycle for the pulsating mode in Figure 13(a). Response frequency determined equal to the forcing frequency similar to the FSREI. Also, the duration of the considered cycle has been chosen from $t = 6.9$ ms to $t = 7.9$ ms, similar to the FSREI. According to the figure, pulsating flames exhibit a milder response to the inlet excitations. Despite the FSREI, there is no considerable change in the flame shape and the flame remains tubular entire the cycle. Temporal variations of the gas-phase temperature along the axis of the microtube during the cycle have been illustrated in Figure 13(b) for pulsating mode. It is obvious that there is no considerable difference between the temperature of different phases on the long side. However, the differences are a little more evident on the short side. The temperature has the highest value at $t = 7.3$ ms and lowest value at $t = 6.9$ ms. In general, temperature amplitude is lower than the FSREI. The maximum temperature difference between the phases was determined to be about 113 K at the short side's outlet.

Diagrams illustrating the axial velocity component along the microtube axis during the pulsating flame cycle are

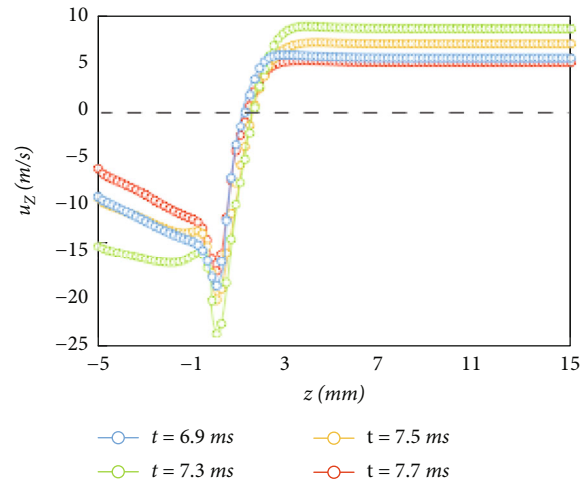

FIGURE 14: Temporal evolution of the axial flow velocity component (u_Z) along the z-axis during a cycle for the pulsating flame mode; $U_{\text{inlet}} = 9$ m/s, $\phi = 0.5$, $A = 0.2$ and $F = 1000$ Hz.

depicted in Figure 14. A dashed line separates positive and negative values. Notably, significant changes are observed near the slots, attributed to the alteration in velocity vector direction resulting from the conversion of inlet circumferential motion to axial motion. In the pulsating mode, there is no reverse flow on the centerline, as indicated by none of the graphs crossing the dashed line on both the short and

long sides. The maximum flow velocity occurs at the instance when the flame reaches its maximum temperature ($t = 7.3$ ms) similar to FSREI. As the incoming flow moves away from the inlet through the long side, the axial velocity stabilizes to a constant value, with a negligible gradient on the centerline. In contrast, the axial velocity exhibits an ascending-descending behavior on the short side. Also, the amplitude of responses is not monotonous on the short side, unlike the long side. Regarding Figures 9 and 14, the maximum response amplitude has appeared at the short side's outlet for both FSREI and pulsating modes. Additionally, the response amplitude increases as the exciting amplitude increases. It happens on both short and long sides.

Temporal variations of the species mass fraction and reaction rates during a cycle have been plotted on the centerline for the pulsating mode in Figures 15 and 16, respectively. Concerning the radicals, changes are not noticeable except near the inlet. The mass fraction increases near the inlet for radicals. As the reactive flow moves downstream, the mass fraction variation becomes negligible. At $t = 7.3$ ms in which flame has the maximum temperature, radicals have their highest mass fraction during the cycle. Also, the minimum mass fraction of the radicals is attained at $t = 6.9$ ms, in which the flame has the minimum temperature during the cycle. The heavier species respond differently. Despite the radicals, fluctuations are more significant at the downstream for the heavier species in the pulsating mode. Fluctuations are more considerable at the long side's downstream. In the diagram of H_2O, the maximum and minimum values of mass fraction occur at the end and beginning of the cycle, respectively. On the short side, the minimum value belongs to $t = 7.3$ ms, in which the short side has the maximum temperature. However, the maximum belongs to $t = 7.8$ ms, in which the gas phase has the minimum temperature. In the diagram of H_2O_2, fluctuations increase on the short side's outlet. The diagram has two peak points, one near the inlet P_1 and the second P_2 on the long side. Position of the P_1 remains unchanged during the cycle, while the P_2 moves towards the long side's downstream. Concerning the HO_2, its diagram exhibits three peak points. The first is P_1 at the $Z = 0.2$ mm, the second is P_2 on the long side, and the third is P_3 on the short side. While the position of the first peak P_1 remains fixed, the second P_2 and third peaks P_3 move upstream and downstream during the cycle. The oscillating behavior of the H_2 is almost similar to the radicals, and most of the incoming H_2 consumes near the inlet. Also, the oscillations of the O_2 are similar to the H_2O.

Due to milder fluctuations, the charts in Figure 16 show less variation compared to those of FSREI (Figure 10). Therefore, charts are displayed for four instances of the cycle. According to Figure 16, R9 exhibits the highest reaction rate throughout the cycle. After that, there are R3 and R1. Subsequently, R8, R1, R2, and R10 have the highest reaction rate, respectively. The order of magnitude for the reaction rates remains consistent over time. Additionally, fluctuations are milder compared to the FSREI. H radical reacts with O_2 in R9 and produces HO_2. At the same time, HO_2 reacts with H in R11 and produces OH. Considering that the change in the rate of R11 is not as intense as the FSREI, OH mass fraction variations are milder in the pulsating mode. Despite the pulsating mode, OH mass fraction tends to zero at the weak and flowing phases in the FSREI mode. Produced OH in the R11 reacts with H_2 in R3 and H in R8, producing H_2O. The reaction R1 progresses in the reverse direction on the short side, where O reacts with OH and produces H and O_2. Also, R1 produces OH and O on the long side and triggers the R3, R8, and R2. This could be caused by the reverse activation of R1, which results in the production of O_2 and H. Produced H in R1 reacts with OH in R8 in the vicinity of another molecule (third body) and produces H_2O. Due to this, the mass fraction of O_2 and H_2O is higher on the short side.

Figure 17 illustrates the variations of response amplitudes of gas-phase temperature and species mass fractions along the axis of the microtube of pulsating mode. Similar to the diagram in Figure 12, species with values of the same order of magnitude are arranged on the same axis. Concerning the temperature, the response amplitude is lower than the FSREI mode, especially near the slots and the short side's outlet. The graph exhibits an ascending-descending trend on the short side, unlike the FSREI mode. At the position $Z = 8$ mm, however, the amplitude of temperature fluctuations is damped, similar to the FSREI mode in Figure 12. According to Figure 17, the amplitude of fluctuations in the OH mass fraction and H_2 mass fractions is negligible in comparison to other species in pulsating mode. However, OH fluctuations were significant in the FSREI mode according to Figure 12. O and H species behave similarly to the FSREI mode, but their fluctuations are lower in the pulsating mode by about two orders. Concerning H_2O_2, amplitudes of fluctuations have the same order of magnitude as OH and HO_2. Amplitudes of fluctuations of H_2O_2 mass fraction grow significantly near the two ends of the microtube in the pulsating mode, but the order of magnitude of the amplitudes is much lower than the H_2O and O_2. The same is true for HO_2.

Fluctuations of O_2 and H_2O exhibit different compared to the FSREI mode. Contrary to the FSREI mode, the response amplitude has lower values near the slots but increases near the outlets. Unlike the FSREI mode, response amplitude increases for H_2O and O_2 on the short side, from the slots to the end. It can be seen from Figures 12 and 17 that H_2O and O_2 are the most affected by inlet excitations, while the effect of inlet excitations on the response amplitudes is at least two orders lower for other species.

3.2.2. Investigation of the Forcing Frequency and Exciting Amplitude. In the present study, the frequency ratio f/F is defined as the response frequency f normalized by the forcing (exciting) frequency F, which is applied at the inlets. Frequency ratio has been calculated over various bulk inlet velocities at different forcing frequencies in Figure 18 for two probe points P_1 and P_2 labeled at $Z = 3$ mm (Figure 18(a)) and $Z = 6$ mm (Figure 18(b)) on the centerline of the microtube, respectively. According to the figure, the effect of the forcing frequency is not evident at $U_{\text{inlet}} = 0.1$ m/s. However, fluctuations become apparent at P_1 as the inlet velocity rises to 3 m/s. Also, the fluctuations are observable for P_2 at $U_{\text{inlet}} = 6$ m/s.

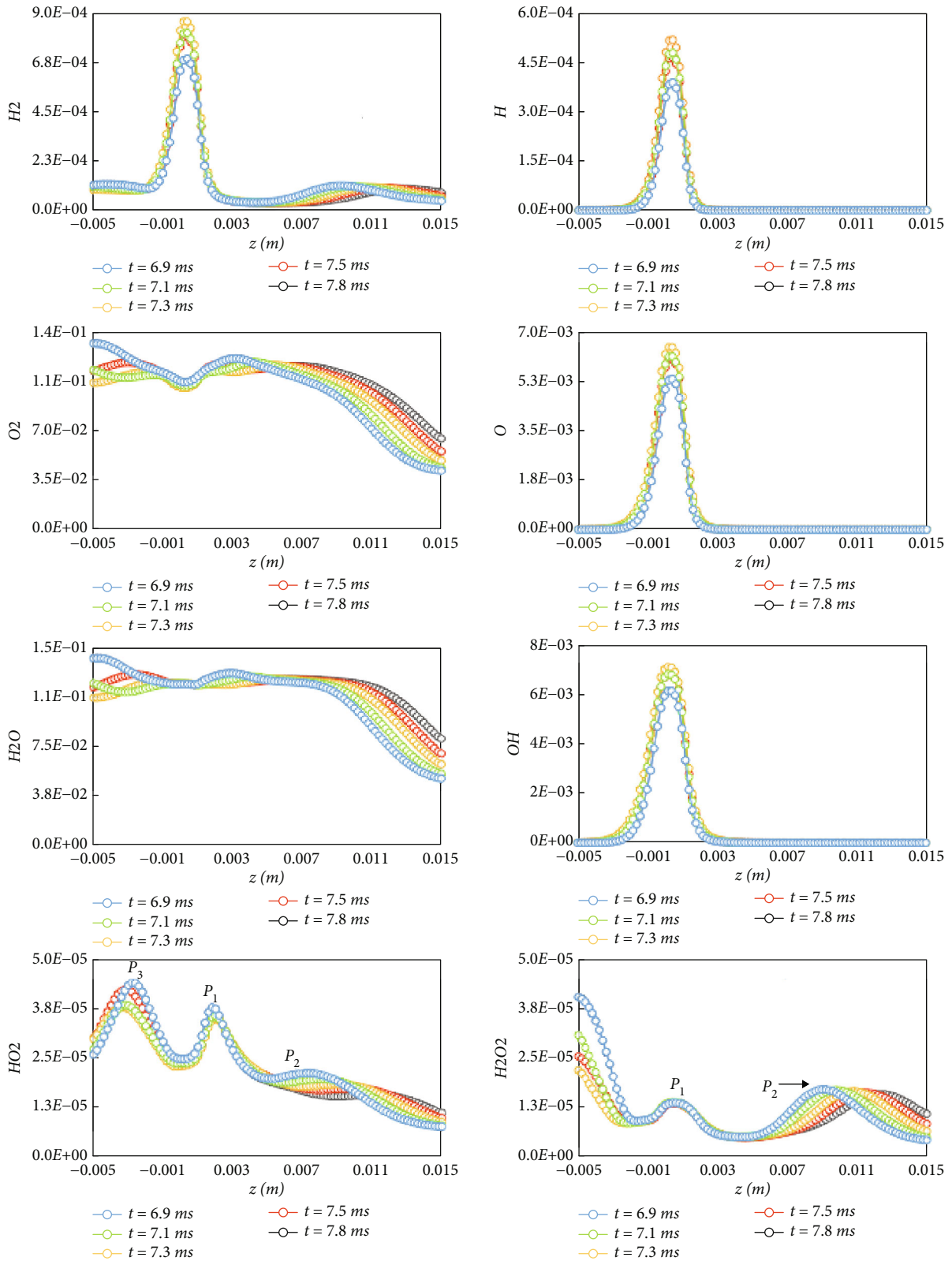

Figure 15: Temporal evolution of the species along the centerline during a cycle of the pulsating flame; $U_{inlet} = 9$ m/s, $\phi = 0.5$, $A = 0.2$ and $F = 1000$ Hz.

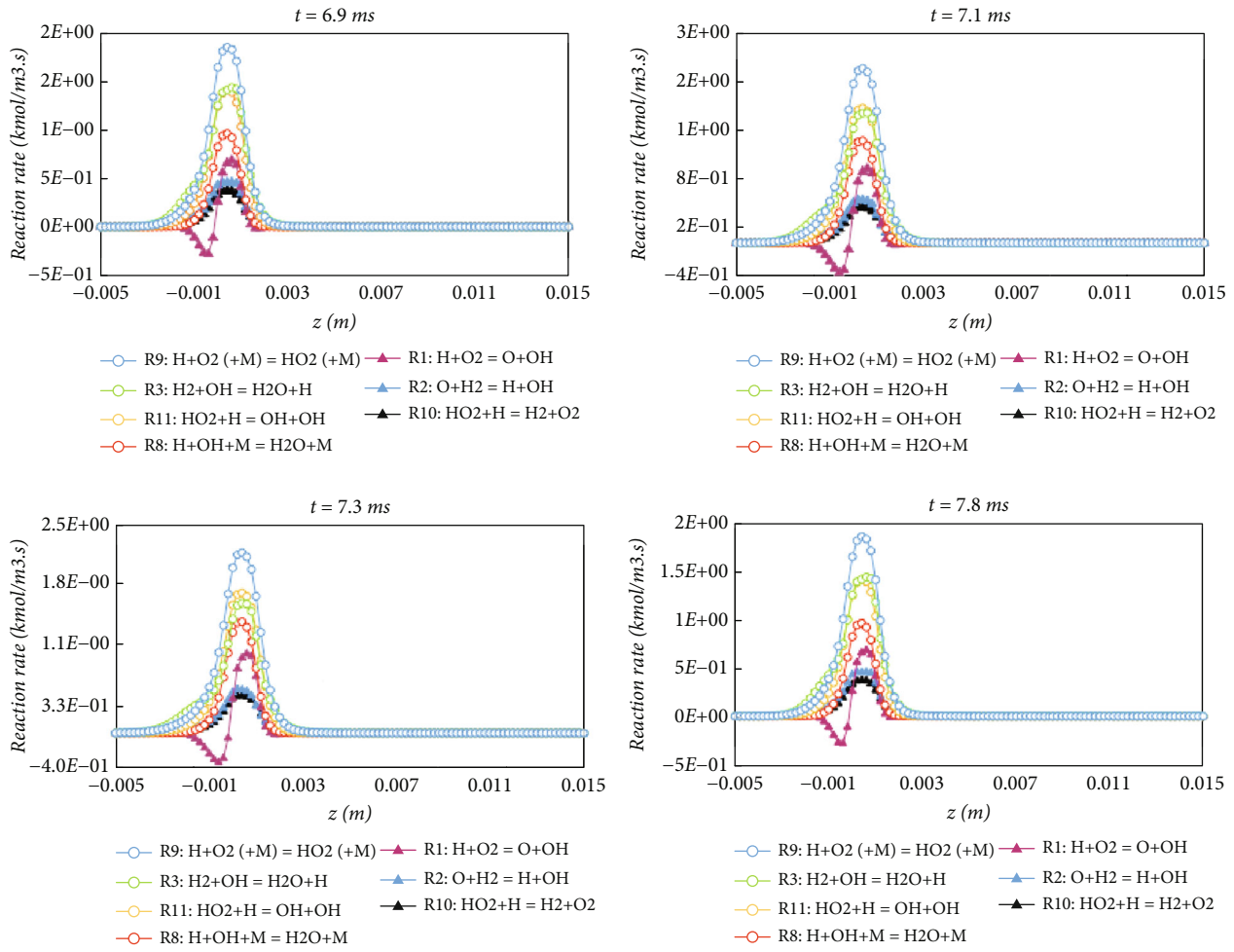

FIGURE 16: Temporal evolution of the reaction rates along the centerline during a cycle of the pulsating flame; $U_{\text{inlet}} = 9$ m/s, $\phi = 0.5$, $A = 0.2$, and $F = 1000$ Hz.

This suggests that fluctuations penetrate to more distant points in the flow by increasing the inlet velocity. However, the inlet velocity increment does not affect the magnitude of response frequency. In fact, the average inlet velocity enhancement only can spread the affected area into the flow field. The frequency ratio decreases by the forcing frequency at a fixed inlet velocity. As the forcing frequency increases to 4000 Hz and 8000 Hz, the frequency ratio drops by half and a quarter, respectively, because the period of the fluctuations drops drastically. Due to the drastically reduced period of fluctuations, it can be compared to flow time and other related phenomena in that the reactive flow is less affected by the inlet exciting frequency.

Figure 19(a) illustrates the response amplitudes of the flow velocity to the inlet excitations, normalized by their average values during a cycle. u' denotes amplitude of the flow velocity fluctuations during a cycle, and U denotes the average velocity during a cycle. u'/U is defined as normalized response amplitude of flow velocity, and its values are calculated in the graph of Figure 19(a) along the microtube axis for different forcing frequencies and exciting amplitudes. According to the figure, the response of the flow velocity to the inlet excitations is more intensive near the slots at $F = 700$ Hz. Amplitudes of the flow velocity fluctuations reach up to two times the average velocity for $A = 1$. By decreasing the exciting amplitude at $F = 700$ Hz, the amplitude of the flow velocity fluctuations decreases near the slots. However, at $F = 1000$ Hz, amplitudes of the flow velocity fluctuations are lower than the average velocity near the slots, and they decrease as the exciting amplitude decreases. The normalized response amplitude increases linearly on the short side for $F = 1000$ Hz and $A = 0.2$. At the exciting amplitudes of 0.6 and 1, variations of the normalized response amplitude have not a clear trend due to the existence of the recirculation velocity fields and negative propagation speed, but it can be concluded that the amplitudes of the fluctuations tend to the average velocity (U) downstream in the short side. Variations of the response velocity are milder on the long side. It decreases by increasing the forcing frequency at a constant exciting amplitude. Moreover, the normalized response amplitude decreases with decreasing the exciting amplitude at a fixed forcing frequency. At $F = 1000$ Hz, normalized response amplitude on the long side equals to its exciting amplitude. This means that the flow velocity is stimulated with the same intensity as the inlet on the long side. However, at $F = 700$ Hz,

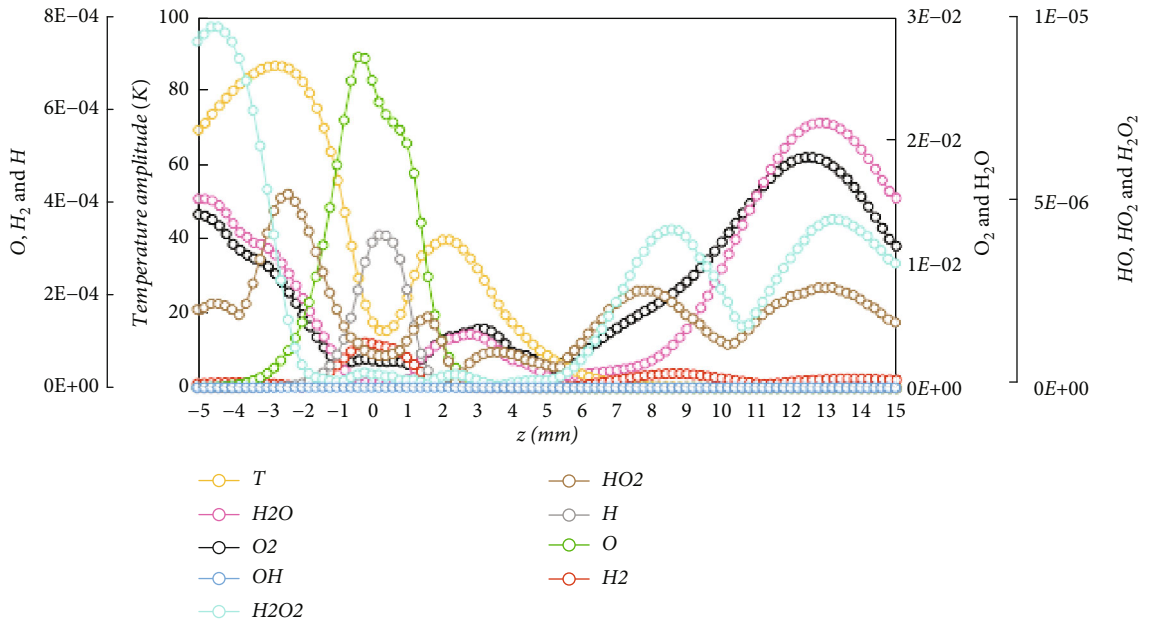

FIGURE 17: Variations of response amplitudes of species mass fractions and gas-phase temperature along the axis of the microtube of pulsating mode; $U_{inlet} = 9$ m/s, $\phi = 0.5$, $A = 0.2$ and $F = 1000$ Hz.

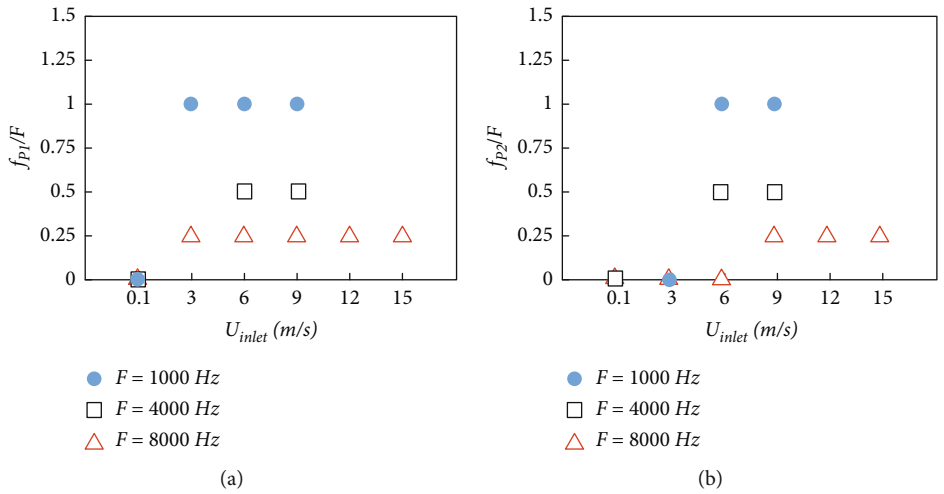

FIGURE 18: Variations of the frequency ratio versus the bulk inlet velocity at different forcing frequencies for (a) P_1 at $Z = 3$ mm and (b) P_2 at $Z = 6$ mm; $\phi = 0.5$ for all cases.

variations of the normalized response amplitude are independent of the exciting amplitude, and it is fixed at 1.4.

Similar to Figure 18(a), the normalized response amplitude of heat release rate (HRR) $\acute{Q}/Q_{avg}$ is calculated for different forcing frequencies and exciting amplitudes along the axis of the microtube. $\acute{Q}$ is the amplitude of the HRR fluctuations, and Q_{avg} is the average value of HRR during a cycle. At $F = 700$ Hz, amplitudes of the HRR fluctuations are at the highest level near the slots similar to the response velocity. As the forcing frequency increases to 1000 Hz, amplitudes of HRR fluctuations are decreased near the slots. Trends of the Q'/Q_{avg} variations with the exciting amplitude are ambiguous on the short side because of the recirculation flow and negative propagation speed, but similar to the normalized response amplitude for velocity, it can be concluded that their valued do not exceed 1 at the outlet. On the long side, for $F = 1000$ Hz and $A = 1$, amplitudes of HRR fluctuations tend to be 1.4 at the outlet, similar to the response velocity. The same is true for $F = 1000$ Hz, and $A = 0.6$. However, the amplitude of the HRR fluctuations is less than the amplitude of the flow velocity fluctuations at $F = 1000$ Hz for $A = 1$ and $A = 0.2$ and at $F = 700$ Hz for $A = 0.6$.

4. Conclusion

The present study investigated H_2/air tubular flame characteristics under stimulated and unstimulated inlet conditions

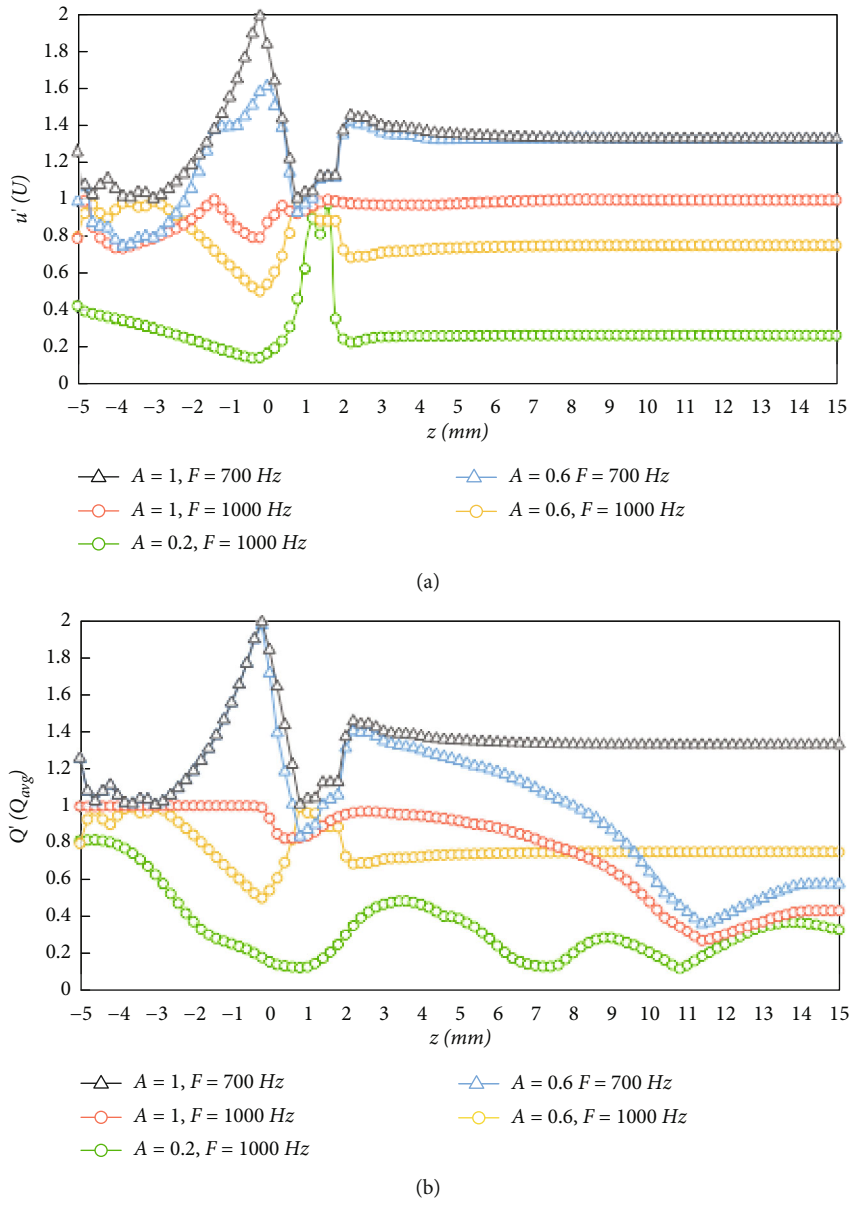

FIGURE 19: Variations of the normalized response amplitude of (a) flow velocity and (b) heat release rate during a cycle for different forcing frequencies and exciting amplitudes along the axis of the microtube; $U_{\text{inlet}} = 9$ m/s and $\phi = 0.5$ for all cases.

in a 1 mm diameter microtube. Based on the results related to the unstimulated inlet condition, it demonstrated promising self-sustaining potential even under blow-out conditions. Inlet velocity enhancement positively influences flow stratification and tubular flame formation. Increasing the centrifugal forces due to the inlet velocity enhancement causes to bifurcate u_r by directing the fresh mixture towards the wall. As a result, the flow becomes well stratified and the temperature gradient of the gas-phase reduces near the wall.

The stimulated inlet conditions revealed two distinct flame propagation modes: FSREI and pulsating flame, observed at different exciting amplitudes. The FSREI mode involved complex phenomena such as recirculation flow fields and negative propagation speed, while the pulsating mode exhibited milder evolution throughout the cycle, never nearing extinguishing conditions and negative propagation speed. A closer look at the FSREI revealed that the reason for the weakening of the flame after the propagation phase is the separation of the flame tips from its kernel due to the difference in the burning speed. The backflow in the flowing phase is forceful enough to prevent dissipation of the released heat in the previous phases. Additionally, increasing the mass flow rate of the fresh mixture causes the lack of excessive time lag between feeding the flame and the heat released in the previous phase. Consequently, unlike the FREI, the flame does not extinguish during the flowing and initiation phases. The pulsating mode experienced a milder evolution during a cycle, and the flame never reached a near-extinguishing condition.

From the kinetic analysis, the reaction $H + O_2 = HO_2$ has the maximum reaction rate during a cycle for pulsating mode. However, in the FSREI, the competition is between $H + O_2 = HO_2$ and $H_2 + OH = H_2O + H$. Response amplitudes of H_2O and O_2 have higher order of magnitude than other species for both propagation modes. Response amplitudes of H_2O and O_2 are the highest near the slots for the FEREI mode and near the outlets for the pulsating mode. As the average inlet velocity increases, inlet excitations affect a wider area of the reacting flow. The response frequency remains 1000 Hz for the forcing frequency of 1000 Hz. However, the response frequency increases to 2000 Hz as the forcing frequency increases to 4000 Hz and 8000 Hz. It seems that the maximum limit of the response frequency is 2000 Hz, and the flame does not respond to the inlet excitations upper than that.

Data Availability

Data are available for request.

Additional Points

Highlights. (i) The radial velocity values are fewer than those attributed to the circumferential velocity by one order. (ii) The average inlet velocity does not affect the magnitude of response frequency. (iii) Due to different time scales, the flame is not completely extinguished in the FSREI mode. (iv) Pulsating flames exhibit a milder response to the inlet excitations. (v) The average inlet velocity enhancement just spreads the affected area into the flow field.

Conflicts of Interest

The authors declare that they have no conflicts of interest.

References

[1] Y. Ju and K. Maruta, "Microscale combustion: technology development and fundamental research," *Progress in Energy and Combustion Science*, vol. 37, no. 6, pp. 669–715, 2011.

[2] G. Pizza, C. E. Frouzakis, and J. Mantzaras, "Chaotic dynamics in premixed hydrogen/air channel flow combustion," *Combustion Theory and Modelling*, vol. 16, no. 2, pp. 275–299, 2012.

[3] G. Pizza, C. E. Frouzakis, J. Mantzaras, A. G. Tomboulides, and K. Boulouchos, "Dynamics of premixed hydrogen/air flames in mesoscale channels," *Combustion and Flame*, vol. 155, no. 1-2, pp. 2–20, 2008.

[4] G. Pizza, C. E. Frouzakis, J. Mantzaras, A. G. Tomboulides, and K. Boulouchos, "Dynamics of premixed hydrogen/air flames in microchannels," *Combustion and Flame*, vol. 152, no. 3, pp. 433–450, 2008.

[5] K. Maruta, T. Kataoka, N. Kim, S. Minaev, and R. Fursenko, "Characteristics of combustion in a narrow channel with a temperature gradient," *Proceedings of the Combustion Institute*, vol. 30, no. II, pp. 2429–2436, 2005.

[6] A. Alipoor and K. Mazaheri, "Studying the repetitive extinction-ignition dynamics for lean premixed hydrogen-air combustion in a heated microchannel," *Energy*, vol. 73, pp. 367–379, 2014.

[7] A. Alipoor and K. Mazaheri, "Combustion characteristics and flame bifurcation in repetitive extinction-ignition dynamics for premixed hydrogen-air combustion in a heated micro channel," *Energy*, vol. 109, pp. 650–663, 2016.

[8] S. S. Minaev, E. V. Sereshchenko, R. V. Fursenko, A. Fan, and K. Maruta, "Splitting flames in a narrow channel with a temperature gradient in the walls," *Combustion, Explosion, and Shock Waves*, vol. 45, pp. 119–125, 2009.

[9] A. Fan, S. S. Minaev, E. V. Sereshchenko et al., "Dynamic behavior of splitting flames in a heated channel," *Combustion Explosion and Shock Waves*, vol. 45, no. 3, pp. 245–250, 2009.

[10] B. Xu and Y. Ju, "Experimental study of spinning combustion in a mesoscale divergent channel," *Proceedings of the Combustion Institute*, vol. 31, no. 2, pp. 3285–3292, 2007.

[11] G. Pizza, C. E. Frouzakis, J. Mantzaras, A. G. Tomboulides, and K. Boulouchos, "Three-dimensional simulations of premixed hydrogen/air flames in microtubes," *Journal of Fluid Mechanics*, vol. 658, pp. 463–491, 2010.

[12] A. Alipoor, K. Mazaheri, and A. Shamooni, "asymmetric hydrogen flame in a heated micro-channel: role of Darrieus–Landau and thermal-diffusive instabilities," *International Journal of Hydrogen Energy*, vol. 41, no. 44, pp. 20407–20417, 2016.

[13] A. Di Stazio, C. Chauveau, G. Dayma, and P. Dagaut, "Oscillating flames in micro-combustion," *Combustion and Flame*, vol. 167, pp. 392–394, 2016.

[14] A. Di Stazio, C. Chauveau, G. Dayma, and P. Dagaut, "Combustion in micro-channels with a controlled temperature gradient," *Experimental Thermal and Fluid Science*, vol. 73, pp. 79–86, 2016.

[15] A. Brambilla, M. Schultze, C. E. Frouzakis, J. Mantzaras, R. Bombach, and K. Boulouchos, "An experimental and numerical investigation of premixed syngas combustion dynamics in mesoscale channels with controlled wall temperature profiles," *Proceedings of the Combustion Institute*, vol. 35, no. 3, pp. 3429–3437, 2015.

[16] P. Abbaspour and A. Alipoor, "Numerical study of combustion characteristics and oscillating behaviors of hydrogen–air combustion in converging–diverging microtubes," *International Journal of Heat and Mass Transfer*, vol. 159, article 120127, 2020.

[17] M. A. Bucci, A. Di Stazio, C. Chauveau et al., "Numerical and experimental analysis of combustion in microchannels with controlled temperature," *Chemical Engineering Science: X*, vol. 4, article 100034, 2019.

[18] C. H. Bhuvan, K. Hiranandani, B. Aravind, V. Nair, and S. Kumar, "Novel flame dynamics in rich mixture of premixed propane-air in a planar microcombustor," *Physics of Fluids*, vol. 32, no. 10, 2020.

[19] I. Schoegl, V. M. Sauer, and P. Sharma, "Predicting combustion characteristics in externally heated micro-tubes," *Combustion and Flame*, vol. 204, pp. 33–48, 2019.

[20] X. Kang, R. J. Gollan, P. A. Jacobs, and A. Veeraragavan, "Numerical study of the effect of wall temperature profiles on the premixed methane-air flame dynamics in a narrow channel," *RSC Advances*, vol. 7, no. 63, pp. 39940–39954, 2017.

[21] S. Mohan and M. Matalon, "Diffusion flames and diffusion flame-streets in three dimensional micro-channels," *Combustion and Flame*, vol. 177, pp. 155–170, 2017.

[22] F. H. Vance, P. de Goey, and J. A. van Oijen, "The effect of thermal diffusion on stabilization of premixed flames," *Combustion and Flame*, vol. 216, pp. 45–57, 2020.

[23] F. H. Vance, Y. Shoshin, J. A. Van Oijen, and L. P. H. De Goey, "Effect of Lewis number on premixed laminar lean-limit flames stabilized on a bluff body," *Proceedings of the Combustion Institute*, vol. 37, no. 2, pp. 1663–1672, 2019.

[24] S. Biswas, P. Zhang, H. Wang, and L. Qiao, "Propagation and extinction behavior of methane/air premixed flames through straight and converging-diverging microchannels," *Applied Thermal Engineering*, vol. 148, pp. 1395–1406, 2019.

[25] H. Nakamura, A. Fan, S. Minaev et al., "Bifurcations and negative propagation speeds of methane/air premixed flames with repetitive extinction and ignition in a heated microchannel," *Combustion and Flame*, vol. 159, no. 4, pp. 1631–1643, 2012.

[26] M. Ayoobi and I. Schoegl, "Numerical analysis of flame instabilities in narrow channels: laminar premixed methane/air combustion," *International Journal of Spray and Combustion Dynamics*, vol. 9, no. 3, pp. 155–171, 2017.

[27] M. Malushte and S. Kumar, "Flame dynamics in a stepped micro-combustor for non-adiabatic wall conditions," *Thermal Science and Engineering Progress*, vol. 13, article 100394, 2019.

[28] S. Lee and B. J. Lee, "Dynamics and stability of premixed hydrogen-air flames in square microchannels with wall temperature gradients," *Proceedings of the Combustion Institute*, vol. 38, no. 2, pp. 1933–1943, 2021.

[29] J. Edacheri, N. Kumbhakarna, and S. Singh, "Effect of hydrogen addition on the dynamics of premixed C1–C4 alkane-air flames in a microchannel with a wall temperature gradient," *International Journal of Hydrogen Energy*, vol. 47, no. 71, pp. 30660–30670, 2022.

[30] F. Ren, H. Chu, L. Xiang, W. Han, and M. Gu, "Effect of hydrogen addition on the laminar premixed combustion characteristics the main components of natural gas," *Journal of the Energy Institute*, vol. 92, no. 4, pp. 1178–1190, 2019.

[31] F. Ren, L. Xiang, H. Chu, Y. Ya, W. W. Han, and X. K. Nie, "Numerical investigation on the effect of CO2 and steam for the H2 intermediate formation and NOX emission in laminar premixed methane/air flames," *International Journal of Hydrogen Energy*, vol. 45, no. 6, pp. 3785–3794, 2020.

[32] L. Xiang, H. Jiang, F. Ren, H. Chu, and P. Wang, "Numerical study of the physical and chemical effects of hydrogen addition on laminar premixed combustion characteristics of methane and ethane," *International Journal of Hydrogen Energy*, vol. 45, no. 39, pp. 20501–20514, 2020.

[33] A. Kunte, A. K. Raghu, and N. S. Kaisare, "A spiral microreactor for improved stability and performance for catalytic combustion of propane," *Chemical Engineering Science*, vol. 187, pp. 87–97, 2018.

[34] W. Zuo, E. Jiaqiang, and R. Lin, "Numerical investigations on an improved counterflow double-channel micro combustor fueled with hydrogen for enhancing thermal performance," *Energy Conversion and Management*, vol. 159, pp. 163–174, 2018.

[35] S. Bani, J. Pan, A. Tang, Q. Lu, and Y. Zhang, "Numerical investigation of key parameters of the porous media combustion based Micro-Thermophotovoltaic system," *Energy*, vol. 157, pp. 969–978, 2018.

[36] M. Ansari and E. Amani, "Micro-combustor performance enhancement using a novel combined baffle-bluff configuration," *Chemical Engineering Science*, vol. 175, pp. 243–256, 2018.

[37] X. Yang, L. Zhao, Z. He, S. Dong, and H. Tan, "Comparative study of combustion and thermal performance in a swirling micro combustor under premixed and non-premixed modes," *Applied Thermal Engineering*, vol. 160, article 114110, 2019.

[38] X. Yang, Z. He, S. Dong, and H. Tan, "Enhancement of thermal performance by converging-diverging channel in a micro tube combustor fueled by premixed hydrogen/air," *International Journal of Hydrogen Energy*, vol. 44, no. 2, pp. 1213–1226, 2019.

[39] X. Yang, W. Yang, S. Dong, and H. Tan, "Flame stability analysis of premixed hydrogen/air mixtures in a swirl micro-combustor," *Energy*, vol. 209, article 118495, 2020.

[40] P. Abbaspour and A. Alipoor, "Numerical study of wavy-wall effects on premixed H2/air flammability limits , propagation modes, and thermal performance of micro combustion chambers," *Applied Energy*, vol. 359, article 122727, 2024.

[41] Z. Mansouri, "Combustion in wavy micro-channels for thermo-photovoltaic applications–part I: effects of wavy wall geometry, wall temperature profile and reaction mechanism," *Energy Conversion and Management*, vol. 198, article 111155, 2019.

[42] Z. Mansouri, "A novel wavy micro-combustor for micro-thermophotovoltaic applications," *Chemical Engineering and Processing-Process Intensification*, vol. 163, article 108371, 2021.

[43] P. Abbaspour and A. Alipoor, "Combustion characteristics of premixed H 2-air in wavy microchannels for micro thermophotovoltaic applications," in *Ninth Fuel Combust. Conf. Iran*, Shiraz, Iran, 2022http://http://fcci2022.shirazu.ac.ir/files_site/files/r_51_220117131412.pdf.

[44] S. Ishizuka, D. Dunn-Rankin, R. W. Pitz et al., *Tubular combustion*, Momentum Press, New York, 2013.

[45] R. J. Kee, A. M. Colclasure, H. Zhu, and Y. Zhang, "Modeling tangential injection into ideal tubular flames," *Combustion and Flame*, vol. 152, no. 1-2, pp. 114–124, 2008.

[46] S. Ren, H. Yang, L. Jiang, D. Zhao, and X. Wang, "Stabilization characteristics and mechanisms in a novel tubular flame burner with localized stratified property," *Energy*, vol. 197, article 117235, 2020.

[47] S. Ishizuka, "Characteristics of tubular flames," *Progress in Energy and Combustion Science*, vol. 19, no. 3, pp. 187–226, 1993.

[48] D. Shimokuri, Y. Honda, and S. Ishizuka, "Flame propagation in a vortex flow within small-diameter tubes," *Proceedings of the Combustion Institute*, vol. 33, no. 2, pp. 3251–3258, 2011.

[49] D. Shimokuri, Y. Karatsu, and S. Ishizuka, "Effects of inert gases on the vortex bursting in small diameter tubes," *Proceedings of the Combustion Institute*, vol. 34, no. 2, pp. 3403–3410, 2013.

[50] N. Hajialigol and K. Mazaheri, "Thermal response of a turbulent premixed flame to the imposed inlet oscillating velocity," *Energy*, vol. 118, pp. 209–220, 2017.

[51] N. Hajialigol and K. Mazaheri, "The dissipation and dispersion of the entropy wave caused by a turbulent lean premixed flame in a combustor," *Applied Thermal Engineering*, vol. 165, article 112900, 2020.

[52] D. V. Thierry Poinsot, *Theoretical and numerical combustion*, R.T. Edwards, Inc., 2nd edition, 2005.

[53] S. R. Turns, *An Introduction to Combustion Concepts and Applications*, McGraw-Hill, 2012.

[54] T. J. Kim, R. A. Yetter, and F. L. Dryer, "New results on moist CO oxidation: high pressure, high temperature experiments and comprehensive kinetic modeling," *Symposium on Combustion*, vol. 25, no. 1, pp. 759–766, 1994.